

Utilization of Soda Ash and its Effect on Fresh and Hardened Properties of Slag-based Mixes

Jayashree Sengupta^{a*}, Nirjhar Dhang^b, Arghya Deb^c

^aResearch Scholar, Dept. of Civil Engineering, Indian Institute of Technology, Kharagpur, West Bengal 721302, India. ORCID: <https://orcid.org/0000-0002-6892-3480>.

^bProfessor, Dept. of Civil Engineering, Indian Institute of Technology, Kharagpur, West Bengal 721302, India.

^cProfessor, Dept. of Civil Engineering, Indian Institute of Technology, Kharagpur, West Bengal 721302, India.

* Corresponding author: jaish.sengupta@iitkgp.ac.in

Keywords: soda ash, hydrated lime, alkali-activated, compressive strength, rheology, thermogravimetric analysis

1. Introduction

It has long been known that natural aluminosilicates can be combined with common limestones to create durable building materials. Roman concrete, which is still regarded as an architectural marvel, is one such example [1], [2]. Following the same grounds, alkali activation of industrial or agricultural by-products, is a recent technological advancement that is valued in order to create a "greener" binder [3], [4]. These "alkali-activated binders," produce concrete that is similar to that made with conventional cement. These exhibit different microstructural compositions based on the raw materials used. Thus, alkali-activation not only helps to value industrial and agricultural wastes but also reduces or even eliminates the need for cement. "No cement" would lower airborne carbon dioxide emissions [5]–[7]. The precursors are essentially non-reactive aluminosilicates that gain binding properties when came in contact with an alkali. When alkalis are added to the system, the aluminosilicates disintegrate releasing the $[\text{SiO}_4]^-$ and $[\text{AlO}_4]^-$ tetrahedral monomers. The excess oxygen is shared by the metal ion and the alumina to create the polymeric gel as these monomers polycondensate to create a three-dimensional network. The polymeric network offers stronger chemical bonds than the CSH gel's layered dreierketten structure, increasing strength. These alkalis are primarily of the alkali metals' group, namely sodium or potassium based, along with a silicate-based solution. A combination of sodium hydroxide and sodium silicate solution is the most typical activating solution [9]. Sometimes, alkali-earth metals, namely calcium and magnesium, is often advantageous in terms of mechanical strength and durability [8].

Despite the benefits listed above, alkali activation has not yet been incorporated into routine concrete practice. This is primarily due to- (i) the need for trained supervision

when using alkalis in solution form (ii) the fact that alkali solutions are highly skin-corrosive and can result in first-degree burns if handled improperly (iii) the use of silicates increases CO₂ emissions and (iv) the cost of the alkalis, which adds to the budgetary burden of construction. One-part mixing is employed to get around the first two limitations, which make use of solid activators and a "just-add-water" strategy. When activators are added as solids, the chemistry changes slightly. Before the aluminosilicates dissociates, the activators are hydrolyzed. Consequently, in one-part mixing, specific factors have an impact on this dissolution. Like the choice and reactivity of the activator being used, as well as the amount of water. Both of which, when combined, should aim an increase in strength. Hence in the present study, it is aimed that the cost of alkali activation did not outweigh its benefits.

Previous studies reported alternative activators from silica-rich wastes like rice husk ash (RHA), ground waste glass (WG) and silica fume (SF) in order to replace the analytical grades of sodium silicate solution that are currently available. These were designed by dissolving the waste products in NaOH or KOH concentrated solutions. The RHA based activator showed similar strength development as the sodium silicate. The possibility that a higher RHA content could affect the mix's flow characteristics shouldn't be discounted, though. Higher RHA tend to significantly increase the yield stress due to higher carbon content, so it should be properly designed. For an equivalent quantity of both materials, the compressive strength with the WG-NaOH activated mix was reported to be higher than a silicate activated mix. On the other hand, the silicate based on silica fume was more effective than the one based on RHA. It was claimed that silica fume benefited from its filling action by creating more calcium silicate hydrates, which increased strength and durability [10]–[13]. With the addition of silica fume, the plastic viscosity was reported to have decreased at higher shear rate aiding to the flowability due to its ball bearing effect [12], [14]. However, any higher amount than 20% resulted in a reduction in strength with the excess amount left unreacted [15]. Also, it increased the volume of large capillary pores [12]. Li et al. [12] reported that the optimal SF amount was about 10%. Sugarcane straw ashes was mixed in NaOH and pre-conditioned for 24 hours to obtain a strength over 50 MPa. Slag produced a strength of 38.38 MPa when combined with olive biomass ash in water. But, for all these silicates derived from wastes, the caustic alkalis were still used in the process, which would still put a strain on the budget. This would also imply that the problem of handling caustic solutions persists. Red mud was used as an alternative to NaOH to activate a fly ash mixture; the results showed that 60% red mud was equivalent to 3–4% of NaOH activated one. However, when using such alternatives, the region-specific availability of such agricultural or industrial waste becomes a constraint.

Given the toxicity of NaOH, Na₂CO₃ and Na₂SO₄ are the milder alternatives. Additionally, they are cheaper. Then again, the shortcomings are, these alkalis are not strong enough to raise the pH of the system to maintain the dissolution mechanisms. Because, presence of CO₃²⁻ ions, tend to delay the dissolution [30]. Despite the lower pH evolution, studies have shown that Na₂CO₃ has the potential to be used as an activator when combined with other additives [36]. Potentially, the reaction could be sped up using Na₂CO₃-activated slag with additions that can regulate the consumption of Ca²⁺. Few studies have looked into the advantages of using both Na₂CO₃ and Ca(OH)₂ as composite activators, namely [9] and [32]. Nevertheless, a combination of Na₂CO₃ and Ca(OH)₂ are more expensive than NaOH alone. Therefore, it has yet to be recognized an activator that is beneficial enough for one-part mixing while also being mild, user-friendly, easily available and cost-effective.

Soda ash is a commonly available industrial product. A significant industrial chemical, soda ash is demanded by a number of sectors including the glass, detergent, paper and chemical manufacturing industries. Additionally, it is used to treat water and as a food additive. The Solvay process creates soda ash by combining carbon dioxide, ammonia, and sodium chloride to create sodium bicarbonate which is then heated to create soda ash. It is widely used all over the world and is easily accessible on the market. In addition to its use in industry, soda ash is also used as a water softener and in some household cleaning products. It is typically regarded as a reliable and safe chemical. Industrial grade hydrated lime is also available for various industrial processes, including water treatment, waste treatment, and construction. In the market, it is offered in a range of purity levels, 75% to 96%, depending on the CaO content. Therefore, using soda ash and hydrated lime as an activator should be able to dissociate a sufficient amount of precursor, though the purity of the chemicals is a topic for investigation.

So far, studies have specified the use of analytical grade chemicals. As the analytical grade indicate higher purity and fineness, it facilitates the reactions. Since industrial grade chemicals like soda ash and hydrated lime have a lower purity than their analytical counterparts, they are less expensive. Hence industrial grade chemicals should be taken up as an alternative activator and investigated for strength development. Mechano-chemical processing was reported to result in early strength development for any structural application. However, any pre-processing would radically affect the cost effectiveness of the alkali activated binders. Hence the dry direct mixing of activators and precursors, following the “just-add water” methodology is adopted here. In addition to the above two requirements, ambient curing method is adopted as heat curing of structural components is almost unworkable on site, energy intensive and disregards the sustainability standpoint of alkali activation.

The present study thus involved mixing the chemicals directly in solid form to the precursors. The effect on fresh and hardened properties are observed. Mixes activated by NaOH pellets pre-mixed in water, are also included for comparison purposes only. The rheological properties, flow characteristics and the strength development are observed for the different types of mixing techniques. Microstructural characterization of selected mortar samples is also performed to support the obtained results of the one-part mixes. The same is not done for the NaOH and pre-mixed activator samples because it is outside the scope of the current study. Finally, the major contributions of the study are summarized. It is anticipated that this alkali-activated slag-based binder would meet the requirements of the construction industry.

2. Research Significance

The goal of the current study is to demonstrate the effectiveness of using industrial grade hydrated lime and soda ash as solid activators to alkali-activate a mixture of slag and silica fume. Different mixing techniques were used, and their influence on the corresponding fresh and hardened properties was examined. Although it was demonstrated in a prior study [32] that a designed NaOH activated mix reached its maximum strength at 6%, the current study did not play around much with the percentage in the same quarter. It was obvious that the mixing technique and the quality of the activators used, namely purity, had a significant impact on the fresh and hardened properties of the mixes. Additionally, Table 1 shows a noteworthy cost difference when using industry grade chemicals. Table 1 also displays the various mixing strategies used (in this paper and otherwise) to highlight how they affected the budget. Using pre-mixed analytical grade Na_2CO_3 in water can cost up to 60% more than using a mixture activated by NaOH pellets. On the other hand, using industrial-grade chemicals could cut down the costs by 91%. Even when compared to analytical Na_2CO_3 counterparts, it saves 94.5% of the budget.

Table 1: Cost comparisons for analytical and industrial grades chemicals for 10% NaOH equivalents of activators for 1m³ of mix

Industrial grade soda ash (as solid or pre-mixed in water) and hydrated lime (as solid)	Analytical grade NaOH pellets in water	Analytical grade Na_2CO_3 and $\text{Ca}(\text{OH})_2$ added in powder form	Measured as	Units
3428.49	39426.60	63115.13	INR	per m ³
Costing Schedule of the materials				
Types	Measured as	Cost	Ref	Form
Analytical grade NaOH	INR per kg	690.00	[16]	Pellets

Analytical grade Na ₂ CO ₃	INR per kg	610.00	[17]	Powder - 99% Purity
Analytical grade Ca(OH) ₂	INR per kg	320.00	[18]	Powder - 99% Purity
Industrial grade Soda Ash	INR per kg	35.50	[19]	Powder - 96% Purity
Industrial grade Hydrated Lime	INR per kg	14.00	[20]	Powder - 90% Purity

3. Material and Experimental Methods

3.1. Material Characterization

Ground granulated blast furnace slag (GGBFS) from Rashmi Cement Limited, West Bengal, India was used as the aluminosilicate precursor. Powdered industrial grade hydrated lime (HL) with 90% purity obtained locally from Shreeram Chemicals Kolkata and soda ash light (SA) from Tata Chemicals Limited with 58.4% Na₂O content were used as activators. Silica fume (SF) was obtained from Walter Enterprises. The SEM micrographs of the precursor and the solid activator as obtained are shown in Figures 1.

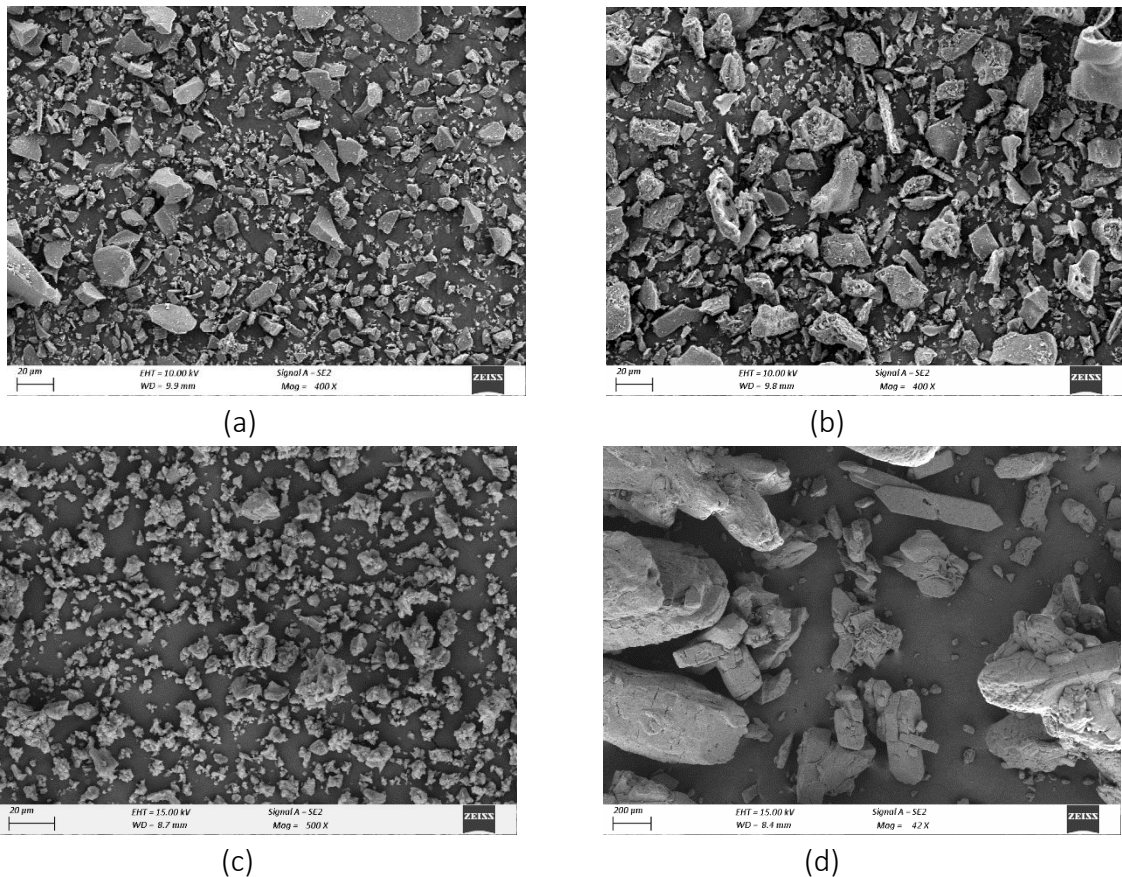


Figure 1: SEM images of the raw materials (a)GGBFS (b) Silica Fume (c) Hydrated Lime (d) Soda Ash

Table 2: Chemical and physical properties of the raw materials

Oxides	GGBFS	SF	HL
--------	-------	----	----

	CaO		43.78	3.81	72.8
	SiO ₂		32.08	84.12	1.47
	Al ₂ O ₃		11.2	0.15	0.87
	MgO		5.82	1.43	1.53
	MnO		0.84	1.15	0.06
Chemical	K ₂ O		0.42	2.7	0.04
Properties	Na ₂ O		0.03	0.02	<0.01
	Fe ₂ O ₃		0.75	2.64	0.36
	TiO ₂		0.87	0.4	0.02
	P ₂ O ₅		1.33	0.72	-
	SO ₃		1.65	0.33	0.15
	LOI		2.74	3.41	25.69
Physical	Appearance		Greyish White	Greyish Black	Pure White
Properties	Density	(kg/m ³)	2890	2170	2240
	Blaine Fineness	(m ² /kg)	385	589	672

The chemical compositions and physical properties of the materials are tabulated in Table 2. For alkali activation, the slag must be either neutral ($B = 1$) or basic ($B > 1$). GGBFS modulus of basicity (B) is defined as the ratio of total basic oxides to total acidic oxides. With a negligible amount of Fe₂O₃, K₂O, Na₂O, and P₂O₅, B equals $(CaO + MgO) / (SiO_2 + Al_2O_3)$. In addition, the GGBFS requires a CaO/SiO₂ ratio of 1.4 (as per BS: 6699) to act as a precursor material. The slag used in this study has $B = 1.14$ and $CaO/SiO_2 = 1.36$, indicating that it can be used as a precursor for alkali activation.

3.2. Mix Proportions

The mortar samples were prepared following the proportions as shown in Table 3. Mortar samples were cast with slag replaced with silica fume at 10% and 20% to study the effect of the additive. The equivalent NaOH % is the targeted amount, that is expected to form when the hydrated lime and soda ash are mixed. Also, it should be so maintained to avoid the presence of unreacted sodium, as one-part mixing is more prone to efflorescence [21]. For example, for 10% NaOH to form, 9.25% ($74/80 \times 10\%$) of hydrated lime and 13.25% ($106/80 \times 10\%$) of soda ash is required. Thus, the corresponding (HL + SA) is set aside as the solid activators, as a percentage of the total of the aluminosilicate material and the additive. The addition of HL in real time raises the system's water demand. Excessive water addition, once again, may lower the pH of the system and impede ionic dissolution. As a result, the water/solids ratio was started at 0.45 and was taken as a ratio of water to total solids, i.e. GGBFS + SF + HL + SA, to facilitate the reaction while also meeting the required water demand. Figure 3 depicts a schematic diagram of the mixing process. For all mixes, the binder: sand ratio was kept constant at 1:3. For casting, standard sand conforming to IS 650-1966 and ASTM C109 was used.

Table 3: Mix proportion of mortars with aggregate: binder as 3:1.

Mix type	Mix ID	Binder (A)		Activators (B)		
		SF %	GGBFS %	(Targeted) NaOH %	Hydrated Lime HL %	Soda Ash SA %
Soda ash and hydrated lime added in solid form	SF10NH6	10	90	6	5.55	7.95
	SF20NH6	20	80			
	SF10NH8	10	90	8	7.41	10.59
	SF20NH8	20	80			
	SF10NH10	10	90	10	9.26	13.25
	SF20NH10	20	80			
	SF10NH12	10	90	12	11.11	15.90
	SF20NH12	20	80			
Control NaOH solution	SF10NH8_C	10	90	8	-	-
	SF20NH8_C	20	80			
	SF10NH10_C	10	90	10	-	-
	SF20NH10_C	20	80			
Pre-mixed soda ash in water	SF10NH8_PM	10	90	-	7.41	10.59
	SF20NH8_PM	20	80			
	SF10NH10_PM	10	90	-	9.26	13.25
	SF20NH10_PM	20	80			



The ratio of molar mass of $\text{Ca}(\text{OH})_2$ to molar mass of 2NaOH is 74/80 and ratio of molar mass of Na_2CO_3 to molar mass of 2NaOH is 106/80.

SF10NH6_C represents 10% of silica fume and 6% of NaOH solution

SF10NH6_PM represents 10% of silica fume and 6% of pre-mixed Na_2CO_3 in water

SF10NH6 represents 10% of silica fume and 6% of equivalent NaOH resulting from the corresponding HL and SA reactions

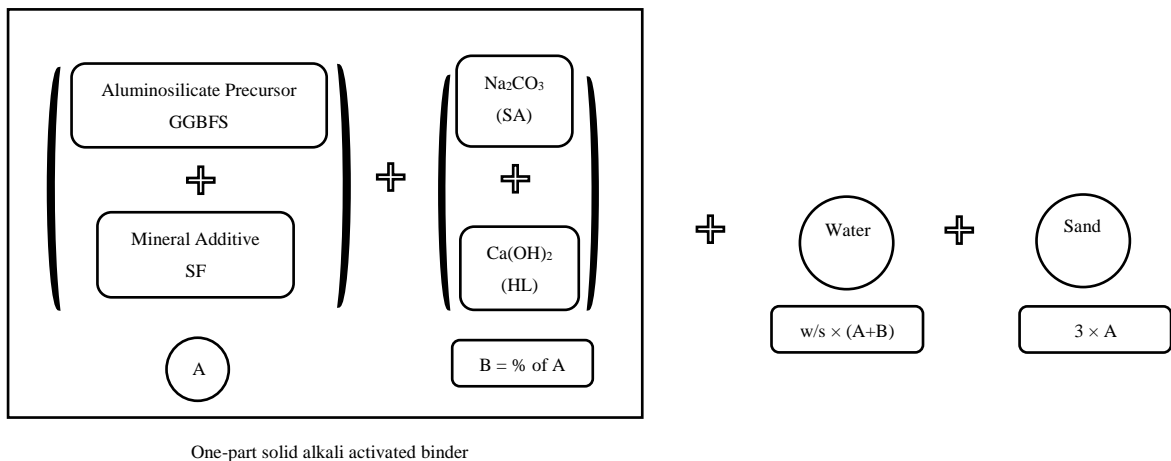


Figure 2: Mixing sequence of the mortar specimens

Table 3 displays the nomenclature for each mix, with SF denoting silica fume and the accompanying number denoting the percentage, and NH denoting sodium hydroxide and the accompanying number denoting the targeted percentage. Therefore, SF10NH6 is equivalent to 10% silica fume and 6% equivalent NaOH. For comparison purposes with

respect to strength development, control mixtures were also tested, activated with analytical grades of solid NaOH pellets pre-mixed in water and is denoted as shown in the table 3. Simultaneously, mortar sample were also tested with industrial grades of soda ash pre-mixed with water and hydrated lime added in powdered form, for similar percentages of selected mixes. All mixing was carried out at room temperature.

3.3. Experimental Methods and Analytical Techniques

3.3.1. Compressive strength test

The mortar samples were cast in 70.6 mm cubic moulds as per IS 4031-6: 1988 and ASTM C109. The solid binder was dry mixed with sand thoroughly for one minute. The water was then added and the blend was mixed for two minutes in a Hobart mixer. The mortar was then placed in the mould on a table of a vibrating machine. While placing, the mortar was prodded 20 times in two layers, to avoid any chances of honeycombing or voids. The period of vibration was set to two minutes. A total of eight mixtures were cast, with nine replicas of each proportion. The samples were demoulded after 24 hours and cured at ambient temperature and 100% relative humidity before testing at 7, 28, and 120 days. Three cubes were tested for each period of curing. Compressive strengths of the mortar samples were determined using a Tinius Olsen Model 120 hydraulic Super 'L' universal testing machine with a load capacity of 60 Ton.

3.3.2. Sample preparation for phase characterization

After the samples were tested for compressive strength, powdered mortar pieces were collected. The samples were dipped in acetone for 45 minutes and then air-dried for 5 minutes. The air-dried samples were then dried in an oven for 2 hours at 60°C. The samples are then taken and kept in a vacuum desiccator until testing for XRD, SEM, and TGA.

3.3.3. Scanning Electron Microscopy- Energy Dispersive Spectrometry

The micrographs of the raw materials and the hardened sample intersections were obtained to have a semi-quantitative chemical composition. As for the hardened samples, the ones with the highest compressive strength were taken up for the microstructural study, XRD, and thermal analysis. The microstructural analysis is done by a field emission-gun scanning electron microscope, with an energy dispersive spectrometer (SEM-EDS, ZEISS Merlin Scanning Electron Microscope with Oxford EDS Detector) was used. Analyses were done using a backscatter electron detector with a 10-kV acceleration voltage. Before testing, the samples were gold coated to have the measurements smoothly. Since

the results are sensitive to point selection, energy dispersive spectroscopy (EDS) analyses of 20 random points were taken on an average, per sample, to determine molar ratios.

3.3.4. X-Ray Diffraction

Identification and quantification of crystalline phases for both the hydrated products (Figure 7) are done. It was performed with XRD using an X'PertPRO PANalytical diffractometer (Cu anode material, K-alpha1 $\lambda = 1.540598 \text{ \AA}$, K-alpha2 $\lambda = 1.544426 \text{ \AA}$). The sample was scanned in the angular range of 5-80° at a step of 2θ , the length of the linear detector being 2.122, and the time per step as 98 sec. XRD analyses were performed on mortar sample powders at the age of 7 and 28 d. The samples were prepared as per section 3.3.2. Quantification of crystalline phases was performed using the Rietveld refinement method in X'PertPRO PANalytical software. The intensities obtained were close-fitted to the X-ray patterns of available models of the crystalline phases in the database, by the least-squares method, which was again obtained by varying the elemental parameters of the peak profiles, to minimize the difference between the observed and the database patterns.

3.3.5. Thermo-Gravimetric Analysis- Differential Thermal Analysis

The mass loss was determined using differential thermal analysis (DTA) and thermogravimetric analysis (TGA) by uninterrupted weight measurement at a constant heating rate. The mass loss provides an indirect approximation of the phases formed by quantification of the bound water and hydroxide phases, and thus the gel formations. Binders undergo thermal reactions that include dehydration, dehydroxylation, decarbonation, oxidation decomposition, phase transition, and melting when heated. These processes are typically followed by weight loss or heat release. In the case of isothermal scenarios, the TGA gives the change in mass as a function of temperature or time at a specific temperature. A thermogravimetric (DTG) derivative weight loss curve allows for better identification of the points where mass losses are most visible. As a result, the portion of moisture and volatile content could be determined by monitoring mass changes. Differential thermal analysis (DTA), on the other hand, distinguishes the heat flux between the sample and an inert reference material and records the phase changes caused by temperature differences. This temperature difference can either be endothermic or exothermic. Most importantly, the measured heat changes indicate the enthalpy change due to loss of water or CO₂ or oxidation or recrystallization reaction [22]. By overlapping the TGA with the DTA curve, the mass loss or gain at specific temperatures could be correlated with the heat flux, to estimate a specific phase and its amount. Through thermal analysis by TGA, one can thus monitor the changes occurring in the mass of the sample owing to the removal of water and decomposition of the hydration products and the polymer network over a range of temperatures. As a result, when TG-

DTG and DTA are analyzed together, they can specify the mass loss at specific temperatures, providing an overview of the undergoing processes and phase formation.

This was done in a Pyris diamond thermal analyser. Samples were collected in powdered form from mortar cubes after performing the compressive strength test. 12-13 mg of the powdered sample with particle size finer than 75 μm was considered for the DTA-TGA. In the experimental setup, the mortar sample was heated from 27°C up to 900°C at a rate of 10°C per minute in an N_2 atmosphere. The powder sample upon heating dissociated to release the hygroscopic water. With further heating, the chemically bound water would also get removed. Thus, by observing the mass loss, i.e. the TG value, the deformation process could be estimated. This was measured in a TG balance of accuracy of 0.1 mg.

4. Results and Discussions

4.1. Compressive strength

Figure 3 depicts the strength development of the samples after 7, 28, and 120 days of curing. SF10NH8, SF20NH8, SF10NH10, and SF20NH10 have higher initial strengths. The 120-day strength of all samples reached a maximum in the same range for both 10% and 20% SF addition. However, the rate of strength gain varied significantly depending on the percentage of silica fume added. This indicated the possibility of a secondary reaction. The initial strength was observed to be more than 20 MPa for a targeted NaOH percentage greater than 6%, while the later-age strength was more than 30 MPa, establishing the competency of the mixes for structural application. Because SF10NH8, SF20NH8, SF10NH10, and SF20NH10 demonstrated the best strength development, with the 28-day strength of 35.1 MPa and the 120-days strength of 41.33 MPa for SF10NH10, these mixes were also prepared for water-to-solids (w/s) ratios of 0.5 and 0.55 using a mixing process similar to that described in section 2.2. Figures 5(a) and (b) depict the strength development of the mixes for other w/b ratios. The compressive strength was reduced as the w/b ratio increased. This was because a higher w/b ratio tended to dilute the system by affecting the $\text{H}_2\text{O}/\text{Na}_2\text{O}$ ratio. As a result, ion dissolution was hampered, resulting in a decrease in strength.

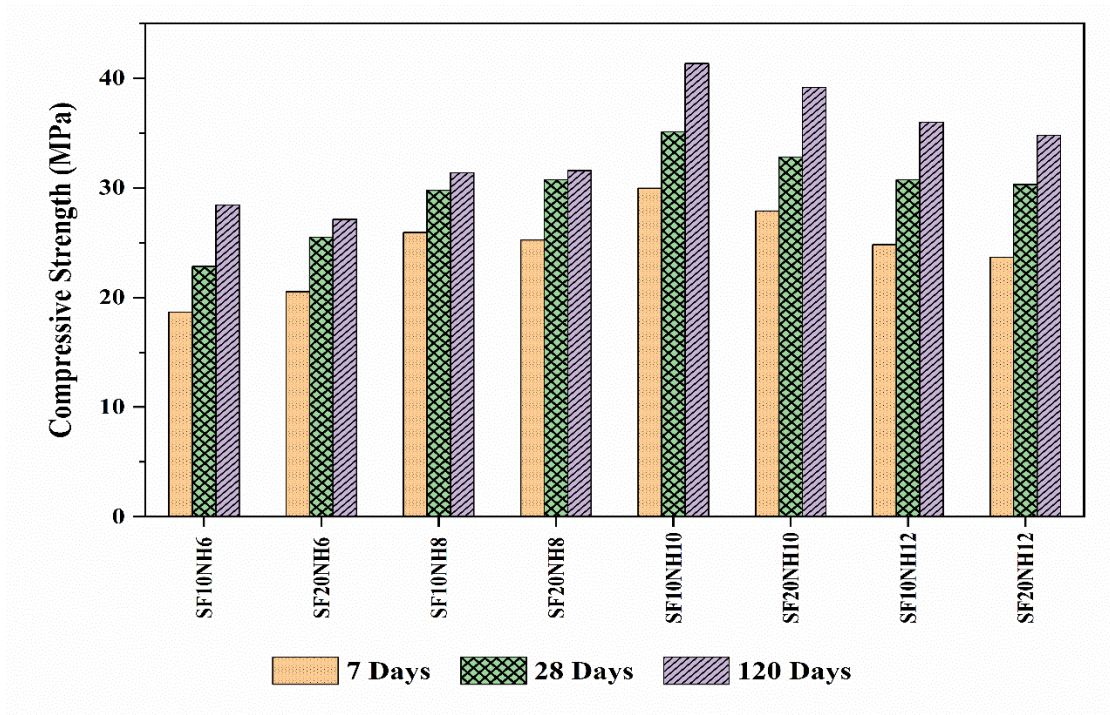


Figure 3: Strength development of various one-part mixes at different ages of curing in sequence of 7, 28 and 120 days.

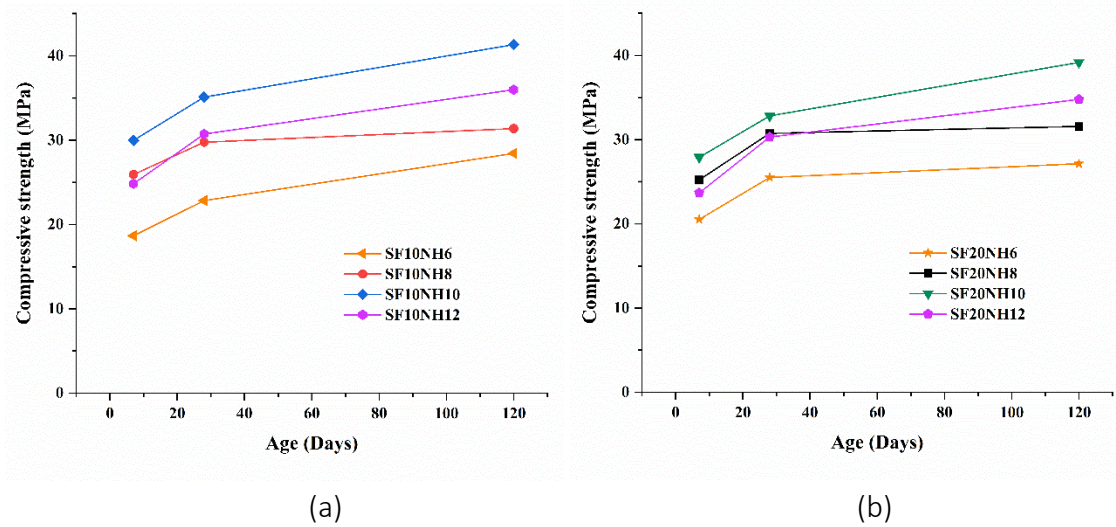


Figure 4: Strength variation of (a) 10% SF and (b) 20% SF addition for different percentages of targeted NaOH

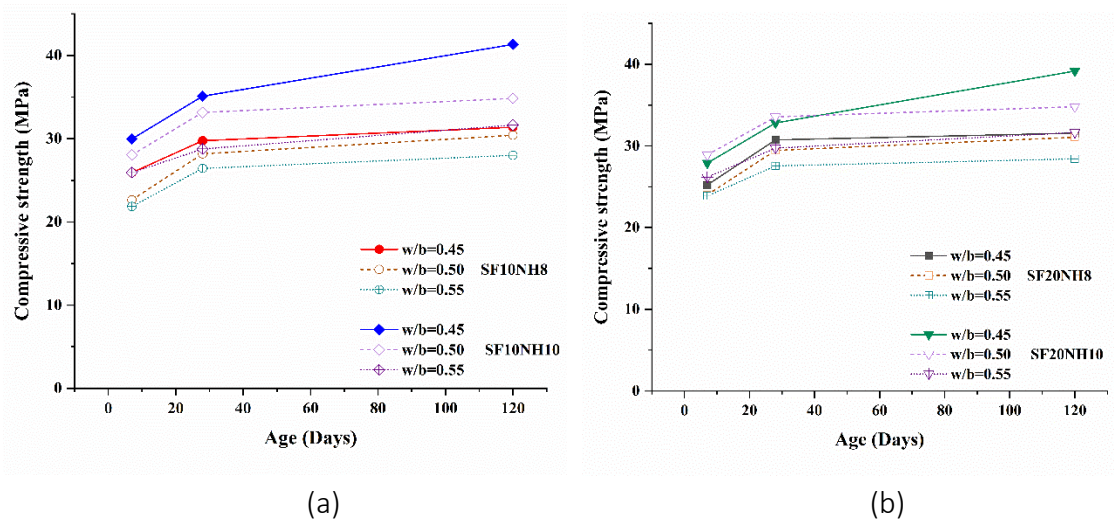


Figure 5: Strength variation of (a) 10% SF and (b) 20% SF addition for 8% and 10% of targeted NaOH respectively at w/s ratios of 0.45, 0.50 and 0.55.

The simultaneous strength development of a NaOH solution activated (control) mix was also tested. The initial strength was noticeably lower than that of the solid activator mixed samples for a 10% NaOH addition, as shown in figure 6. The initial strength was reduced as the sodium content was increased. However, the later age strength improved considerably. The rate of strength gain was not systematic for the samples, though. This could be attributed to the competition between the Na^+ and Ca^{+2} ions, due to Lewis acidity, hindering the reaction. In addition, a pre-mixed soda-ash solution was used to activate a GGBFS-SF-calcium hydroxide mix, and the initial strength development was high, in line with the previous studies [23]. This could be because the system was activated solely by soda ash, while hydrated lime acted as an additive. Bernal et al. [24] reported slow activation by Na_2CO_3 , where the primary reaction formed gaylussite, which then formed calcite and hydrotalcite. The hydrated lime mostly balanced off the CO_3^{-2} ions in the pore solution in the pre-mixed soda-ash solution blends. A higher 28-day strength was observed for the pre-mixed soda ash mixes. In all cases, though, 10% SF and 10% NaOH (direct as well as equivalent) showed the maximum strength development. In the current study, advantageous strength development in the solid-state mixes demonstrated that the underlying chemistry contributed to the benefits of the same. This one-part mix had a higher initial strength than the mixes activated by the NaOH solution, however lesser than a pre-mixed soda ash mix. Although a targeted NaOH incorporation resulted in a CaCO_3 presence, it contributed to the strength enhancement. This is consistent with the findings of [25], who found calcite formation to be a stable polymerization product in a Na_2CO_3 activated fly ash mixture. CaCO_3 filling was reported beneficial with reduced porosity [26]. Additionally, after 120 days of curing, there was a subsequent improvement.

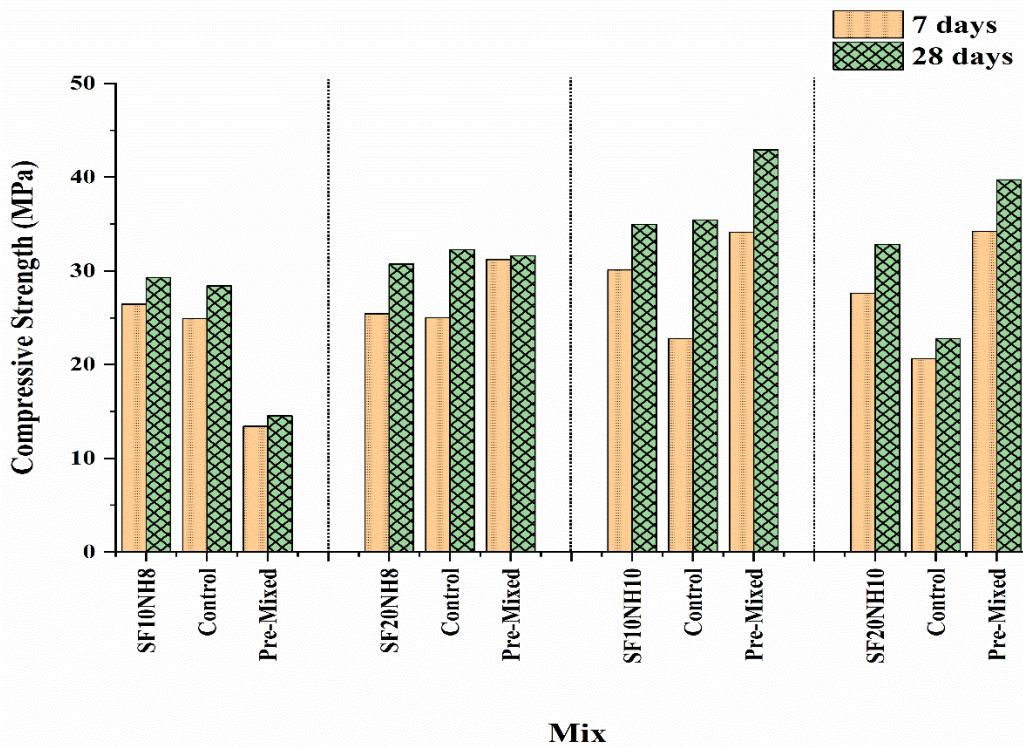


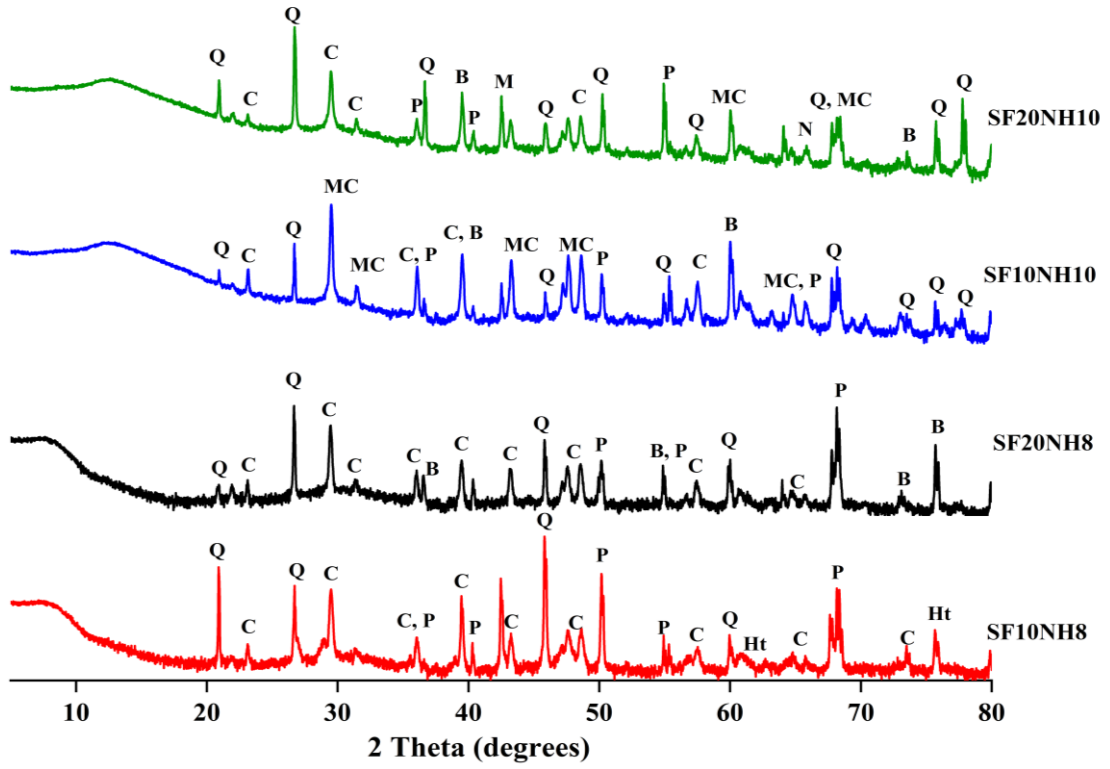
Figure 6: Strength comparison of the mixes, the equivalent Control NaOH solution activated mix and the Pre-mixed soda ash in water activated mix at w/b ratios of 0.45.

4.2. Phase Analysis through XRD

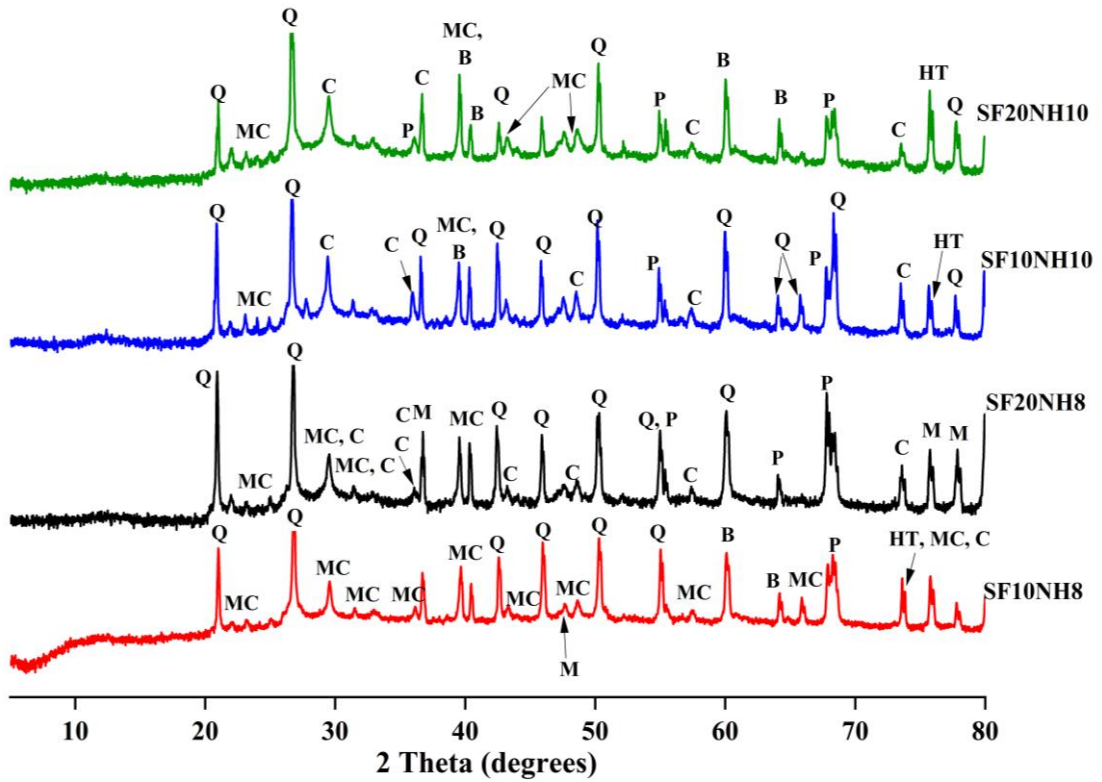
The mixes with the highest strength were chosen for microstructural analysis. As a result, SF10NH8, SF20NH8, SF10NH10, and SF20NH10 were chosen. The phases formed are identified using X'Pert Highscore Plus v3.0. Figure 7 depicts the main reaction products. N-A-S-H (Zeolite X, Ca- exchanged, #98-001-2576), C-N-A-S-H (Zeolite A, #98-002-2602), calcite (#00-005-0586), mineral portlandite (#98-005-8830), brucite (#98-003-5306), gibbsite (#98-012-3163), and quartz (#00-033-1161) were detected. The degree of irregularity in the pattern could be interpreted as it diffracted the X-rays. In an amorphous state, the diffraction of X-rays resulted in broadly diffused halo rather than sharp diffraction peaks. The broad and amorphous convexity, centered at around 27–29° (2θ) was the characteristic peaks of amorphous gels including zeolitic gels and calcium silicate hydrate gels, typical of the diffraction pattern of alkali-activated materials [27]–[29]. The more convex, the more the strength. It indicated that the alkali activation reaction and the hydrate reaction occurred at the same time. Most of the peaks in XRD resulted from quartz and calcite. The calcite formation resulted from the initial cation exchange reaction between soda ash and hydrated lime; resulting in the formation of sodium hydroxide and calcium carbonate. Calcium carbonate is also reported to prevent the formation of ettringite [30]. The intensity of the calcite peaks was observed to have decreased at 28 days of diffractograms. The decreased intensity of the calcite peaks could be explained by the simultaneous formation of magnesites and magnesian calcites at 28

days. The presence of brucites was detected in the 7-day sample but not in the 28-day sample. Brucites most likely reacted with calcite to form portlandite and magnesite over time. It almost certainly aided in the formation of the C-N-A-S-H with the supplied Ca^{+2} ions. The same is supported by the detection of C-N-A-S-H in the XRD of all 28-day samples, which was absent in the 7-day sample. Unlike [31], the presence of gaylussite (hydrated sodium-calcium carbonate) was not found in the XRD.

Portlandite diffraction peaks were observed in all samples of all ages. However, the intensity dropped significantly at 28 days. The portlandite (mineral) could have been the unused inorganic calcium hydroxide i.e. the hydrated lime, that was initially supplied to the system; however, the simultaneous formation of calcite ensured the formation of sodium hydroxide, and the presence of portlandite (mineral) was probably a secondary reaction product. The formation of C-A-S-H and C-S-H could explain why the peak's intensity was reduced. Tobermorite 14 A was identified in all samples, along with zeolite X (Ca- exchanged and Na- exchanged), with no obvious strong peaks indicating its amorphous nature. Specific trona peaks in SF20NH10 were observed, indicating the presence of unreacted sodium carbonate. All samples exhibited zeolite A (C-N-A-S-H) at 28-days. Thaumassite peaks (98-007-9112) were also detected in the 28-day samples. The differential thermal analysis also confirmed the presence of thaumasite. Hydrotalcite characteristic peaks (98-000-6182) were also observed in SF10NH8 at 7 days, but not in other samples. However, a hydrotalcite peak was observed in all 28-day samples with a d-spacing of 1.25 Å and 75.78(2). Brucite peaks were also detected in all samples, with the intensity decreasing or disappearing after 28 days.



(a)



(b)

Figure 7: XRD of the mortar samples at (a) 7 days (b) 28 days. Q= Quartz; P= Portlandite; C= Calcite; B= Brucite; M= Magnesite; MC= Magnesian Calcite; HT= Hydrotalcite

4.3. Microstructural Characterization

Figure 8 and 9 shows the scanning electron micrographs of the 28-day sample respectively. Cubic crystal formations were observed to have formed in the 7-day samples. SF10NH8 showed scattered micro-cracks. Some cracks were observed which were a result of the heat treatment before testing as vacuum drying could cause cracks to appear [32]. Calcite crystallized as a result of the initial ion exchange reactions and can be seen in the images of the 7- day samples. SF20NH10 had a calcite-rich microstructure after 7 days of curing. Furthermore, the XRD revealed the presence of NaOH, confirming the presence of unreacted aluminosilicates. After 28 days of curing, the microstructures developed into dense and compact systems. It is clear that SF10NH10 had a developed microstructure, which is consistent with the strength development results.

To provide compositional and elemental mapping, EDS was performed simultaneously. The EDS revealed that the major elements in most cases were Ca and Si, with moderate contributions from Na, Mg and Al and minor contributions from Mn and Fe. The formation of CSH gel was primarily influenced by major elements. Ca, Na, and Al was responsible for the simultaneous formation of CASH and NASH. Mg contributed to the formation of brucite at 7 days, magnesite and magnesian calcite and hydrotalcite at 28 days, as shown by the XRD. So far, the experimentally obtained molar ratios are shown in table 4. The elemental ratios represent free ion concentrations in the pore solution, such as $[Na^+]$, $[Al^{+3}]$, $[Si^{+4}]$, $[Mg^{+2}]$, $[Ca^{+2}]$, $[OH^-]$, and so on. As a result, the elemental concentration should decrease with age as the reaction progressed. The table 4 shows the EDX data for an average of 20 points. Any inconsistency would point to the presence of unreacted particles. The same can be said for SF20NH10, where the Na concentration was much lower, indicating slower dissolution. As the corresponding $[Al^{+3}]$ concentration indicated, this had a direct impact on slag particle dissolution. Since, slag was the sole source of $[Al^{+3}]$ ions. As a result, the Al/Si ratio dropped to 0.01 and the Na/Si ratio dropped to 0.005, indicating incomplete aluminosilicate dissolution. SF10NH10, on the other hand, demonstrated a greater reduction in $[Al^{+3}]$ concentration (36%) at 28 days, indicating greater Al^{+3} ion engagement. Abdelrahman et al. [33] suggested that increasing the Na/Al ratio, which was the primary contributor to the formation of N-A-S-H, increased the degree of reaction until a certain point, after which saturation was reached and any increase in Na/Al had no significant effect on the reaction kinetics. However, SF20NH8 demonstrated a higher strength development (21.84% increase) for a comparatively

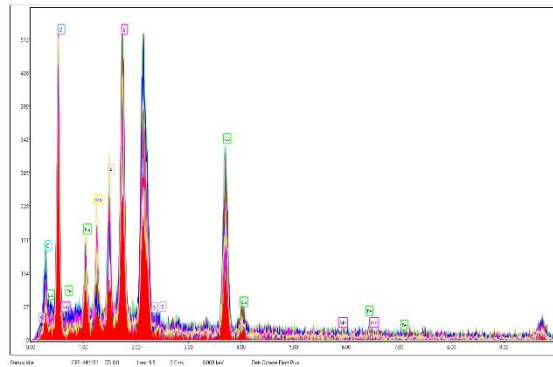
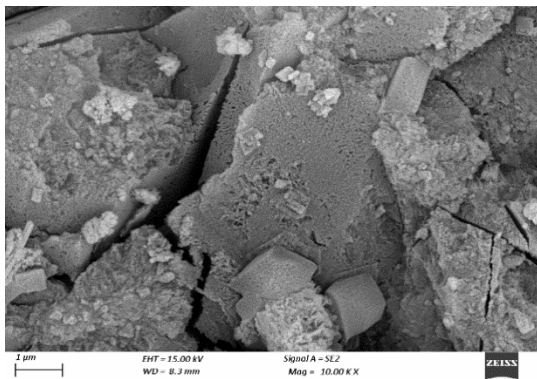
lower increase in the Na/Al ratio (52.48%). The extra strength was most likely due to the coexistence of C-A-S-H and C-S-H, both of which had been reported to co-occur [8]. C-A-S-H and C-S-H were both affected by the decreasing Ca/Si ratio [34]. The strength of SF10NH10 was 35.1 MPa, with the corresponding Na/Al increasing by 76.88% and the Ca/Si decreasing by 43.12%, supporting the co-existence theory of the gels as reported in [8]. The preceding statement was also supported by the formation of Tobermorite 14A in XRD, as well as Zeolite A and Zeolite X.

Table 4: Experimental molar ratio of selected mixes

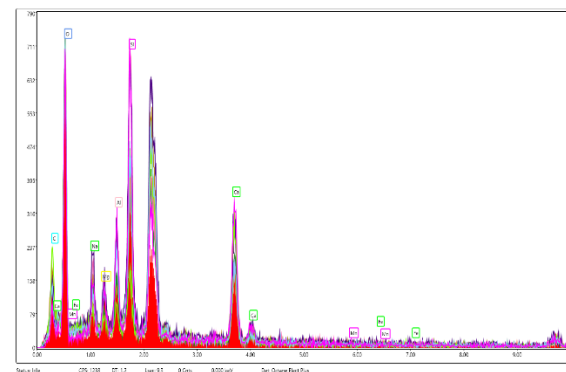
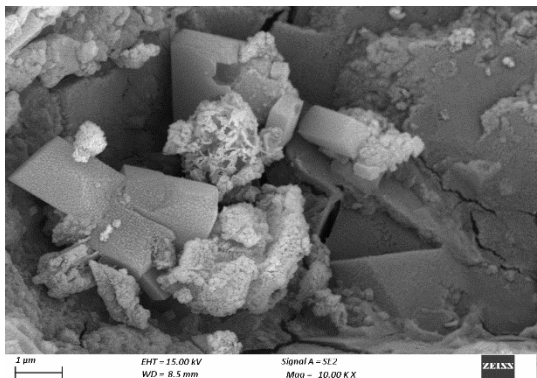
Mix	7 days									Compressive strength		
	C	O	Na	Mg	Al	Si	Ca	Mn	Fe			
SF10NH8	4.72	23.00	4.48	3.14	8.40	24.31	26.66	1.52	1.62	25.93		
SF20NH8	6.85	29.45	2.18	2.55	6.17	18.85	29.17	1.17	1.44	25.23		
SF10NH10	4.52	26.39	4.36	0.29	12.39	20.22	29.00	1.37	1.89	29.97		
SF20NH10	7.28	14.21	0.23	0.12	0.51	48.94	26.62	1.23	0.87	27.9		
Mix	28 days									Compressive strength		
	SF10NH8	13.56	21.46	4.64	2.43	7.01	18.41	16.76	12.87		0.11	29.76
	SF20NH8	6.29	13.08	2.16	2.91	5.99	23.85	21.58	20.62		0.16	30.74
	SF10NH10	19.07	16.16	5.53	3.63	7.93	20.87	17.03	15.71		0.15	35.1
	SF20NH10	8.24	26.73	3.51	1.47	4.40	24.57	21.92	9.13		0.04	32.82

It should be noted that the Na/Ca for SF10NH10 increased by 116% after 28 days. Additional Ca^{+2} ions, which was confirmed by the reduced portlandite and calcite peaks in XRD, appeared to have played an important role in the formation of C-N-A-S-H and C-S-H. In a $\text{Ca}(\text{OH})_2$ or CaCO_3 system, the presence of Mg^{+2} in the form of magnesium hydroxide could result in the formation of magnesium-containing carbonate [35] and the liberation of additional Ca^{+2} ions. These were also seen in the XRD in the present study, with brucite detected at 7 days and magnesite detected at 28 days. This was proportional to the Mg/Ca ratio [35]. Adding reactive MgO to GGBFS blends had been shown in studies to increase mechanical strength via the formation of hydrotalcite [36], [37]. The formation of the hydrotalcite-group and AFm-type phases is governed by the amount of freely available Mg, which has a significant impact on the chemistry of the C-(N)-A-S-H gel [38]. In $\text{Mg}(\text{OH})_2$ and Na_2CO_3 activated mixtures, the formation of gaylussite was followed by the formation of calcite and hydrotalcite [39]. The presence of hydrotalcite could be confirmed by comparing the Mg/Al ratio [40], [41] for mineral hydrotalcite, which gave a range of 2-3. In the current study, the Mg/Al ranged between 0.2 and 0.5 for all samples, confirming the lesser intensity of hydrotalcite as observed in the XRD. Due

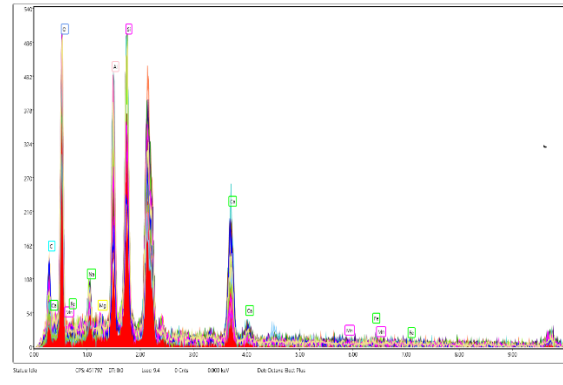
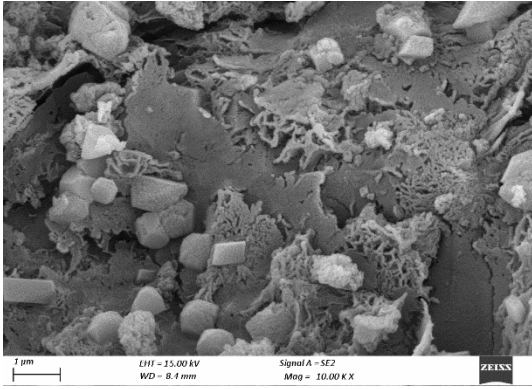
to strong solvation shells of Mg and an intrinsic crystallization barrier, the reaction of $\text{Mg}(\text{OH})_2$ with ambient CO_2 was much lower than that of $\text{Ca}(\text{OH})_2$ [42]. However, it had been reported that the presence of carbonates causes M-S-H phases to form much more quickly, destabilizing brucite. This primarily developed when silica fume reacted with magnesium oxide or hydromagnesite found in an environment rich in sodium carbonate with a Mg/Si ratio of 1.5 [43]–[45]; however, the ratio in the current study was much lower, so this might not be the case. At room temperature, however, brucite in an alkaline medium of NaOH and carbonated portlandite could precipitate magnesium-calcite and/or (hydrated) magnesium carbonate [42]. The main carbonate phases in this case were magnesium carbonate phases, as the Mg/Ca ratio increased [35]. It was likely the same phenomenon was occurring here, so the decrease in calcite peaks and magnesite formation was accompanied by the formation of water molecules, explaining why SF10NH10 has a higher strength despite having a higher amount of free water as determined by the following TG-DT analysis. At 28 days, the Mg/Ca for SF10NH10 increased noticeably. The decrease in calcite peaks in XRD ensured that more Ca^{+2} was available for any secondary pozzolanic reactions, explaining the 116% increase in the Na/Ca ratio. The presence of magnesian calcite in all samples also suggested that this occurred.



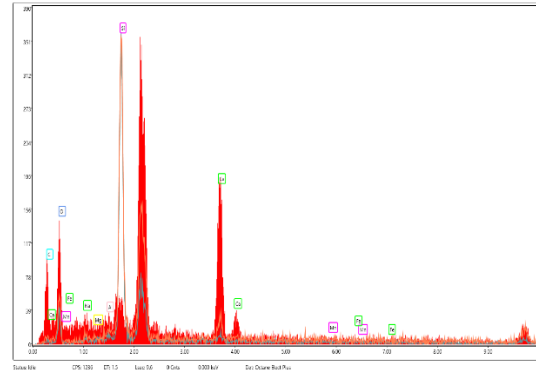
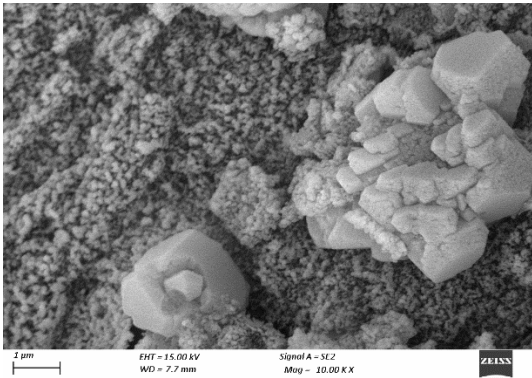
(a)



(b)

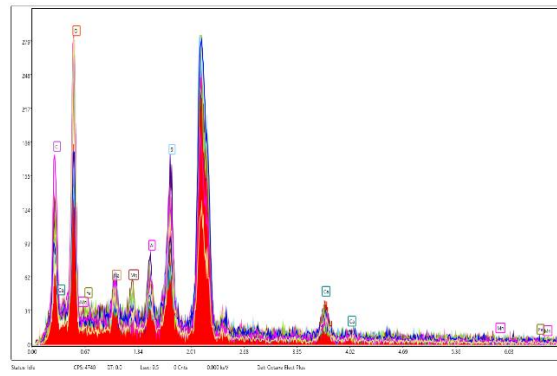
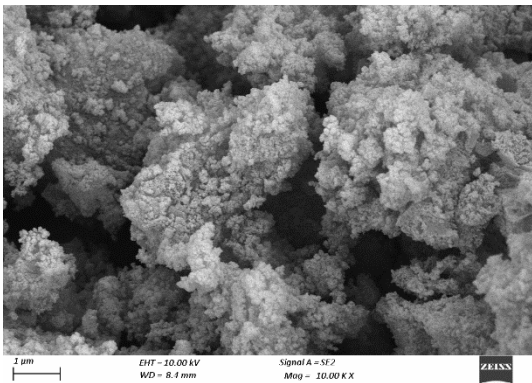


(c)

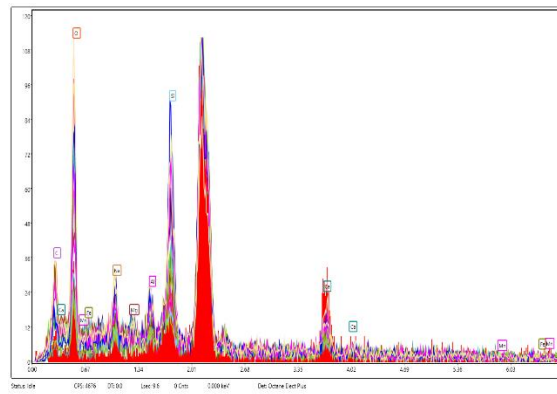
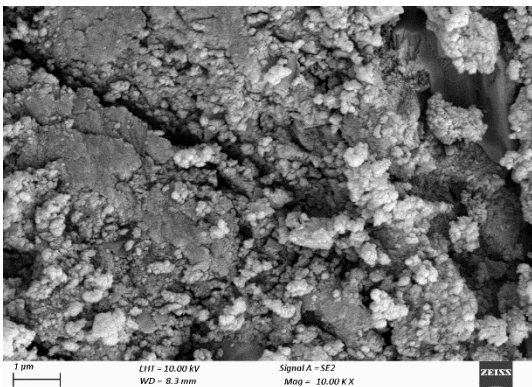


(d)

Figure 8: SEM images of mortar at 7 days containing (a) SF10NH8 (b) SF20NH8 (c) SF10NH10 (d) SF20NH10



(a)



(b)

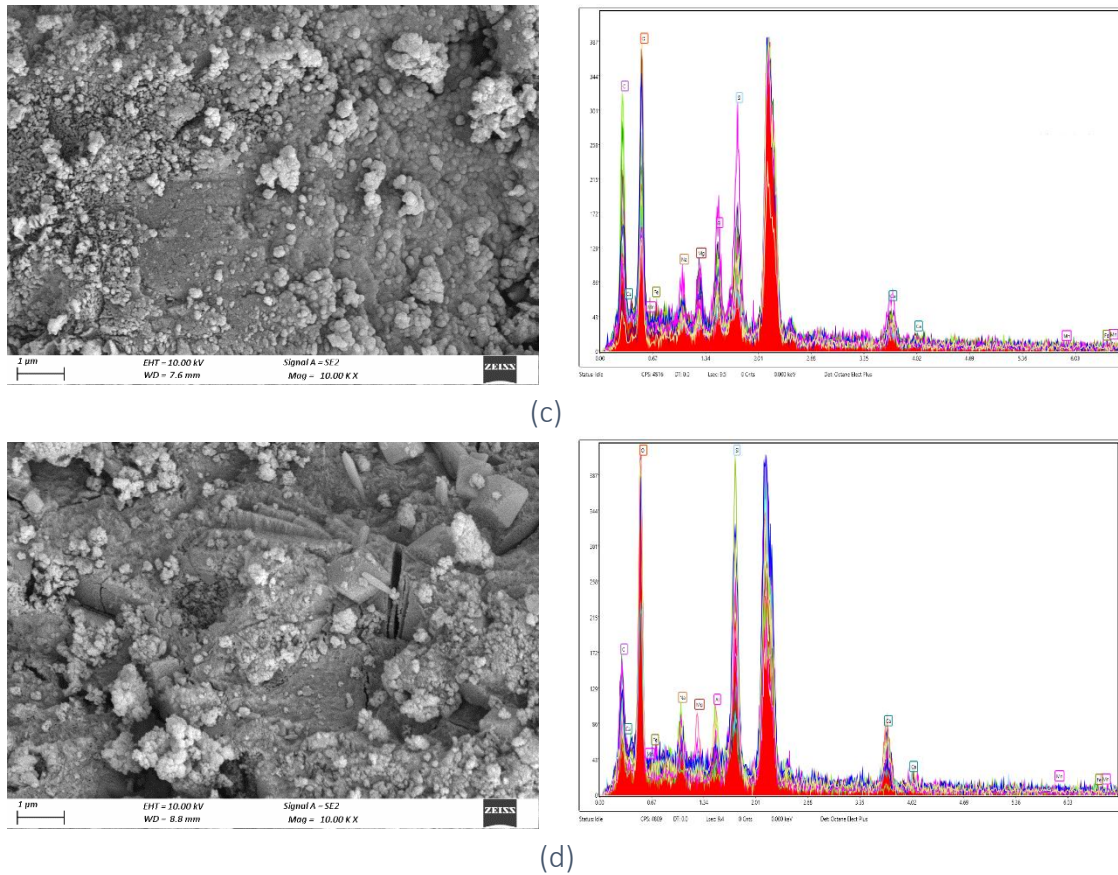


Figure 9: SEM images of mortar at 28 days containing (a) SF10NH8 (b) SF20NH8 (c) SF10NH10 (d) SF20NH10

4.4. Thermal Analysis

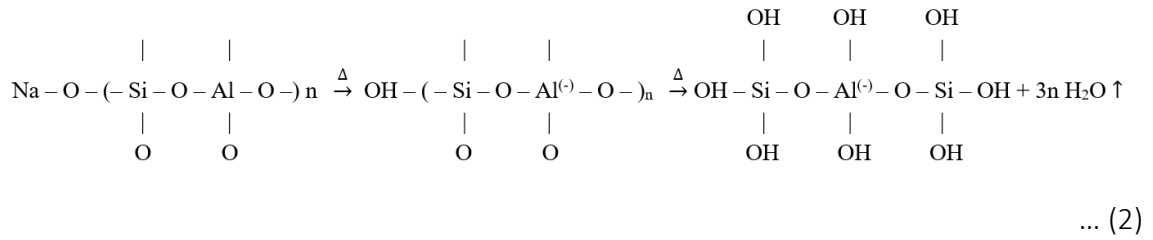
4.4.1. Phase Transitions

At 28 days, Figure 8 depicts the DTG curves of SF10NH8, SF20NH8, SF10NH10, and SF20NH10. Figure 8 depicted the DTG thermograms of the endothermic peaks; as they returned to the baseline, each decomposition step was grouped. The temperature ranges were identified as 32°C to 105°C, 105°C to 150°C, 150°C to 230°C, 230°C to 420°C, 420°C to 635°C, and 635°C to 800°C based on the peak in the curve. These endothermic peaks corresponded to the different compositions as confirmed by XRD after 28 days of curing-

(1) Dehydration (Ldh) of the water molecules: This sub-categorized in the curve as-

- free and hygroscopic water removed up to 105°C but not considered bound water [46], [47]
- crystalline water removal from thaumasite formation ($\text{Ca}_2\text{Si}(\text{OH})_6(\text{CO}_3)(\text{SO}_4^-) \cdot 12\text{H}_2\text{O}$; Aft phases as observed in XRD) at around 105°C to 150°C.

- intra-layer water from CSH [48], CASH, and NASH (structural hydroxyl group) at 150°C to 230°C [49], [50].

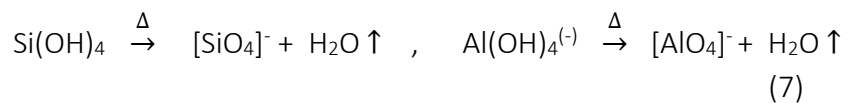
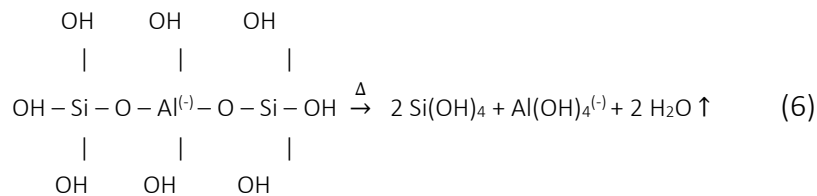


(2) Dehydroxylation (Ldx) of metal hydroxides and the inter-layer [OH⁻] group remained in the alkali-activated system. This phase could be divided into two sub-types –

- Dehydroxylation of gibbsite (aluminum hydroxide) (245°C [51]) and brucite (magnesium hydroxide) (330°C [52]) took place between 230°C to 420°C. It is to be noted that SF10NH8 and SF20NH10 showed prominent endothermic peaks at 270°C showing the decomposition of hydrotalcite.



- Dehydroxylation of Portlandite (around 480°C [53]–[55]) and decomposition of the oligomers, formed in eq. (1), into monomers took place between 420°C and 635°C.



(3) The third phase was characterized by decarbonation (Ldc) of carbonates (calcite, magnesite, and magnesian calcite) from 635°C to 800°C.

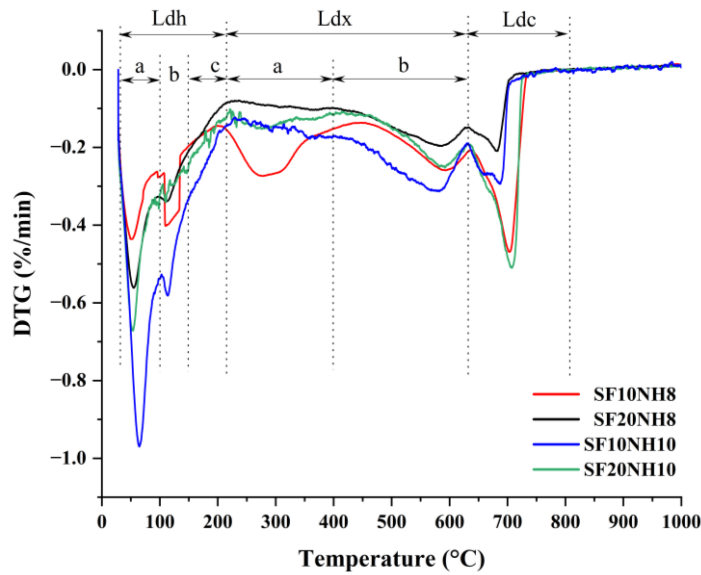
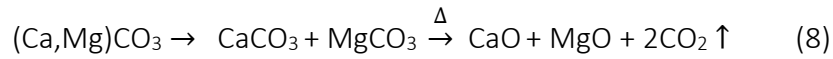


Figure 10: DTG curves of mortar at 28 days of SF10NH8, SF20NH8, SF10NH10, SF20NH10

When compared to the corresponding DTA, the first endotherm was observed at A in the DTA curve. This was due to evaporation of free water. This peak was more pronounced for SF10NH10 at 71°C, indicating the presence of more hygroscopic water in the sample. A second endotherm related to the breakdown of the thaumasite phase was observed at around 116°C. A slight change in the slope was observed at C, indicating the start of decomposition of polymeric gels, particularly C-A-S-H type gels, around 180°C [56] liberating OH⁻ ions to the system. A prominent exotherm was observed beyond C, which was most likely the result of a consecutive decomposition of the CSH and the portlandite phases. The loss of inter-layer water of C-S-H started around 200°C [57], [58]. Ca(OH)₂ dehydroxylation occurred near 460 °C via CaO + H₂O, and large amounts of CaO had been reported to be produced [59]. The same was observed for the raw hydrated lime- a sharp endothermic DTG peak around 435°C. In their study [59], the starting temperature was 400 °C, and as the temperature increased, the intensity of Ca(OH)₂ decreased while the intensity of CaCO₃ increased. As a result, the exotherm at D corresponds to the oxidation and carbonation occurring. Around 573°C, an endothermic peak was observed at E, which was attributed to the β-α quartz transformation in the sand [53], [60]. The characteristic amorphous profiles of C-S-H began to change from 615°-630 °C, according to Song et al.

[59]. A similar upward exotherm was observed in the DTA curve for all samples at around 635°C due to crystallization. A simultaneous endotherm-exotherm was observed between 690°C and 715°C. This was likely the result of magnesium calcite [61] decomposing into magnesia, lime, and carbon dioxide. Lime, on the other hand, was more reactive to carbon dioxide than magnesia [42] and quickly formed a more stable calcite, which then decomposed.

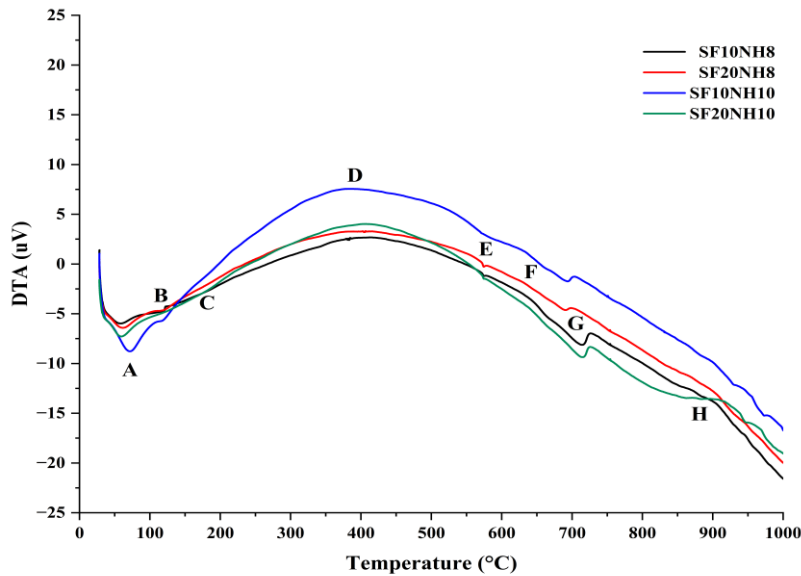


Figure 11: DTG curves of mortar at 28 days of SF10NH8, SF20NH8, SF10NH10, SF20NH10

4.4.2. Significance of TG-DTA Results

TG-DTA, in addition to providing an overview of the phases decomposing at specific temperatures, also provided an amount of the bound water associated with the phase decompositions. Because the volatiles were primarily bound water and CO₂, evaluating the mass changes over different temperature ranges could provide an overview of the bound water. As a result, the bound water evaluation indirectly provided an indication of the associated gel formation. So far, there are few methods in the literature for estimating the bound water and degree of hydration in cementitious mixes [62]–[65]. Table 5 summarizes the temperature ranges associated with the three major phases from the previous section. Despite the fact that other methods were considered distinctly on cement binders, the ranges in this paper corresponded to those obtained from the alkali-activated samples' DTG-DTA curves. While Bhatti [62] and Pane et al. [63] methods strictly adhered to cement binders, Monteagudo's [64] and Deboucha's [65] methods incorporated additive supplemented binders to calculate the bound water. Bhatti's method accounted for mass loss between 105°C and 1000°C, but did not account for carbonation due to anhydrous material in the presence of unreacted particles. They included a conversion factor of 0.41 due to the carbonated portlandite, which was also present in the DTA of the current study at peak 'E'. This value corresponded to the

molecular weight ratio of H₂O and CO₂ [66]. Similarly, an additional conversion factor of 0.41 was considered in this study to allow carbonated brucite forming magnesite, as observed in the XRD. Pane et al. [63] corrected for anhydrous unreacted materials' additional carbonation. They did not, however, include the conversion factor for portlandite carbonation. Monteagudo [64] combined both methods and arrived at a common expression for portlandite and anhydrous material that included both factors. Deboucha [65] incorporated the mineral additive's influences via two major effects: filler and chemical effect, and mass drift. A modified Deboucha method is thus used here, to estimate the bound water associated with each selected sample.

Deboucha had already incorporated additives and considered their effect on hydration kinetics. Both Deboucha [65] and Bessa [67] stated that the additive influences hydration kinetics via the filler effect and the chemical effect. As Deboucha pointed out, additive materials aided in hydration through the synergy of dilution and heterogeneous nucleation in cementitious binders. In one-part alkali-activation, which was largely governed by hydrolysis in the underlying chemistry, similar phenomenon occurred. Furthermore, the additional secondary hydration products must be counted as a chemical effect. Keeping these two possibilities in mind, chemical activators in solid form aided in the nucleation of the precursor grains and should thus be considered. The device drift considered by Deboucha and proposed by Mounanga was not considered here because the operator reported negligible heating of the crucible.

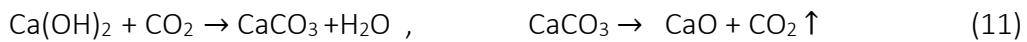
$$W_B = Ldh + Ldx + 1.025(Ldc - Ldc_a) - (m_{precursor} \times LOI_{precursor} + m_{additive} \times (LOI_{SF} + LOI_{SA} + LOI_{HL})) \quad (10)$$

$$m_{precursor} = \frac{m_s - m_b \left(x_{SF} + x_{SA} + x_{HL} + \frac{W}{B} \right)}{1 + LOI_{precursor}} ;$$

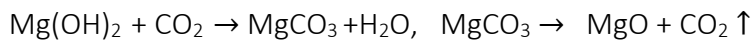
$$m_{additive} = \frac{m_s - m_b \left(x_{GGBFS} + \frac{W}{B} \right)}{1 + LOI_{SF} + LOI_{SA} + LOI_{HL}}$$

$m_s, m_b, x_{SF}, x_{SA}, x_{HL}, \frac{W}{B}, LOI_{SF}, LOI_{SA}, LOI_{HL}$ are the initial mass of the sample, and total binder mass, all considered as the equivalent of 1gm of sample, the replacement level of the additives (mineral and chemical), the water/binder ratio, and the loss on ignition of the additives (mineral and chemical) respectively. It was assumed that the activators completely react with water to kick off the dissolution. The expressions of various methods are summarized in table 9.

While evaluating the bound water, it should be noted that a carbonate salt had already been introduced into the system. As a result, whenever the mass loss due to decarbonation of carbonated portlandite was estimated ($Ldc-Ldc_a$), a portion of calcite from the initial ion exchange was also recorded. According to the intensity reduction of calcite and formation of additional magnesium calcite, from the XRD, and the DTA readings, $Ca(OH)_2 + CO_2$ did occur, but the rate of reaction was subdued by other reactions occurring concurrently. Only then the XRD intensity reduction of calcite was justified. In addition, given the significant participation of magnesium, as per the XRD observations, an additional factor of 0.41 was also included. Unlike calcite decomposition, magnesite formation was solely the result of brucite carbonation. As a result, magnesite decarbonation was accounted for by ($Ldc- Ldc_a$). However, a correction factor was required to account for both carbonated portlandite and calcite produced by ion exchange. Thus, the weight fraction of calcium carbonate (as balancing off the stoichiometry of the initial ion exchange) was subtracted from the total correction factor to directly evaluate the bound water associated with portlandite. For example, for SF10NH8, balancing the stoichiometry in eq. 1, a weight fraction of 10% of calcite was produced. Hence a correction factor of 0.925 (= [1.025-0.1]) was used for the estimation of ($Ldc- Ldc_a$). The following equations (11-13) explain the total correction factors. And the corrected bound water is evaluated in table 10.



$$W_{B \text{ carbonated } CH} = \frac{W_{mH_2O}}{W_{mCO_2}} \times Ldc = 0.41 Ldc,$$



$$W_{B \text{ carbonated } MH} = \frac{W_{mH_2O}}{W_{mCO_2}} \times Ldc = 0.41 Ldc \quad (12)$$



$$W_{B \text{ carbonated } MH} = \frac{W_{mH_2O}}{W_{mCO_2}} \times Ldc = \frac{0.41}{2} Ldc = 0.205 Ldc \quad (13)$$

Hence total correction factor is 1.025 ($Ldc- Ldc_a$). The values are shown in table 10.

Table 5: The temperature ranges as per different authors

Phase Transitions	Free and Bound Water		Temperature Ranges				
			Bhatty	Pane and Hansen	Montegaudo et al	Deboucha et al	Present Study
Free and hygroscopic	Dehydration	Free water	--	--	--	--	32°C to 105°C
Crystalline water removal		Ldh	105°C to 440°C	140°C to 440°C	105°C to 410°C	105°C to 400°C	105°C to 150°C
Chemically bound water							150°C to 230°C
Decomposition of aluminum hydroxide	De-hydroxylation	Ldx	440°C to 580°C	440°C to 520°C	430°C to 530°C	400°C to 600°C	230°C to 420°C
Decomposition of Portlandite							
Decarbonation of calcite	Decarbonation	Ldc	580°C to 1000°C	520°C to 1100°C	530°C to 1100°C	600°C to 1000°C	635°C to 1000°C

Table 6: The mass variations with temperature for the anhydrous materials

	GGBFS	SF	SA	HL
Mass weight at 105° C	10945.2253	14627.3584	14241.13	5433.272
Mass weight at 635° C	10860.1317	14306.9814	14219.17	4110.166
Mass weight at 1000° C	10708.356	14170.3682	13521.13	4082.571
LdCa	1.387	0.934	4.902	0.508

Table 7: Evaluation of Ldc_a for different mixes

	SF10NH8	SF20NH8	SF10NH10	SF20NH10
GGBFS	90	80	90	80
SF	10	20	10	20
Na ₂ CO ₃	7.4	7.4	9.25	9.25
Ca(OH) ₂	10.4	10.4	13.25	13.25
Ldc _a (%)	1.889	1.843	2.038	1.993

Table 8: Weight of sample at different temperatures

Mix	W _{32°} (μg)	W _{105°} (μg)	W _{150°} (μg)	W _{230°} (μg)	W _{420°} (μg)	W _{635°} (μg)	W _{1000°} (μg)
SF10NH8	12866.57	12539.35	12364.07	12205.64	11715.84	11187.45	10825.05
SF20NH8	12454.08	12062.84	11910.97	11788.55	11576.26	11167.40	11037.15
SF10NH10	12408.41	11791.61	11544.55	11345.30	10998.91	10347.33	10137.07
SF20NH10	12547.22	12123.28	11967.29	11813.33	11518.06	11047.50	10671.72

Table 9: The expressions for evaluating bound water content as per different authors

Methods	Expressions
[62]	$W_B = Ldh + Ldx + 0.41Ldc$
[63]	$W_B = Ldh + Ldx + (Ldc - Ldc_a)$
[64]	$W_B = Ldh + Ldx + 0.41(Ldc - Ldc_a)$
[65]	$W_B = Ldh + Ldx + 0.41(Ldc - Ldc_a) - (m_c \times LOI_{cc} + m_A \times LOI_{AC}) + m_d$ $m_c = \frac{m_{sample} - m_B \left(x + \frac{W}{B} \right)}{1 + LOI_c} ; \quad m_A = \frac{m_{sample} - m_B \left[(1 - x) + \frac{W}{B} \right]}{1 + LOI_A}$
Present Study	$W_B = Ldh + Ldx + 1.025(Ldc - Ldc_a) - (m_{precursor} \times LOI_{precursor} + m_{additive} \times LOI_{additive})$ $m_{precursor} = \frac{m_s - m_b \left(x_{SF} + x_{SA} + x_{HL} + \frac{W}{B} \right)}{1 + LOI_{precursor}} ;$ $m_{additive} = \frac{m_s - m_b \left(x_{GGBFS} + \frac{W}{B} \right)}{1 + LOI_{SF} + LOI_{SA} + LOI_{HL}}$

Table 10: Evaluation of bound water content WB as per different studies

Mix	Free water Ldh _a (%)	Ldh (%)		Ldx (%)		LdC (%)	LdC _a (%)	Bhatty (%)	Pane and Hansen (%)	Monte-gudo et al. (%)	Present Study (%)
		Ldh _b	Ldh _c	Ldx _a	Ldx _b						
SF10NH8	2.543	1.398	1.264	3.906	4.214	2.890	1.898	11.966	11.773	11.188	10.578
SF20NH8	3.141	1.259	1.015	1.760	3.389	1.080	1.853	7.866	6.650	7.106	5.408
SF10NH10	4.971	2.095	1.690	2.938	5.526	1.783	2.038	12.979	11.994	12.144	10.783
SF20NH10	3.379	1.287	1.270	2.436	3.882	3.100	1.993	10.145	9.981	9.328	8.802

In addition to evaluating the bound water, the hydroxide phases could also be evaluated from the TG-DT analysis. Authors [64], [65] assessed free portlandite through the following equation, deriving from the stoichiometry of the equations (11-13).

$$CH_{free} = \left(\frac{74.09}{18.01} \right) Ldx_b + \left(\frac{74.09}{44.01} - \%_{calcite} \right) (Ldc - Ldc_a) \quad (14)$$

where, $\left(\frac{74.09}{18.01} \right)$ is the molar mass ratio of Ca(OH)₂ to water, $\left(\frac{74.09}{44.01} \right)$ is the molar mass ratio of Ca(OH)₂ to CO₂ and $\%_{calcite}$ is the weight fraction of calcium carbonate as balanced off the stoichiometry of the initial ion exchange. Similarly, free gibbsite and free brucite

could be evaluated as follows. To avoid overestimation, the weight fraction of calcium carbonate was subtracted in both assessments [65].

$$MH_{free} = \left(\frac{58.32}{18.01}\right) Ldx_a + \left(\frac{58.32}{44.01}\right) (Ldc - Ldc_a) \quad (15)$$

$$AH_{free} = \left(\frac{78}{18.01}\right) Ldx_a - MH_{free} \quad (16)$$

Table 11: Summary of CH, MH, AH, free water and bound water and the corresponding strength

Mix	Free MH	Free AH	Free CH	Free Water	Bound Water	28-day Strength (MPa)	120-day Strength (MPa)	Increment in strength
SF10NH8	27.51	10.59	18.91	2.54	10.58	29.76	31.37	5.41
SF20NH8	15.73	8.11	12.72	3.14	5.41	30.74	31.57	2.70
SF10NH10	27.10	14.38	22.34	4.97	10.78	35.10	41.33	17.75
SF20NH10	21.78	11.24	17.69	3.38	8.80	32.82	39.17	19.35

Table 11 thus displays the corrected bound water and hydroxide estimations. SF10NH10 had the highest concentrations of free water, bound water, and hydroxides. While SF10NH8 and SF20NH8 showed only a minor difference in 120-day strength development, there was a significant improvement in strength gain for 10% SF samples. Similarly, the NH10 samples showed a higher strength gain. Higher MH also ensured the formation of magnesium calcite and hydrotalcite [42], which added to the strength and thus a higher strength gain. This also promoted the formation of water molecules, which explained why SF10NH10 has a higher strength despite having more free water. Previous research [68] reported that the AH phase formation could be expressed as a function of pH. Higher AH in NH10 samples might thus indicate a higher pH.

5. Conclusions

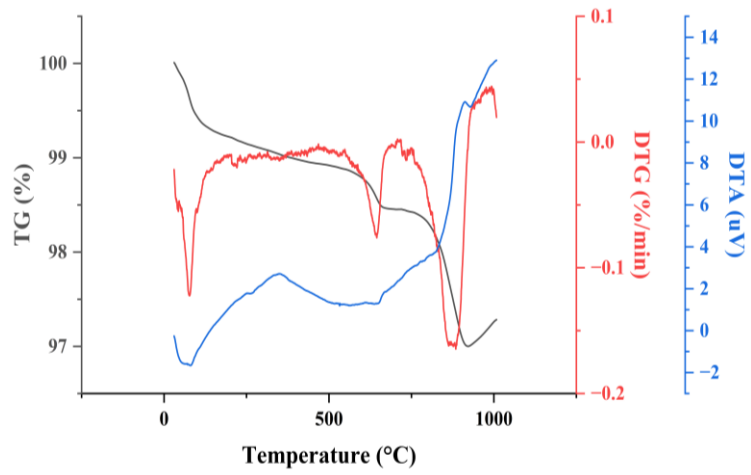
To be deemed as a cost-effective binder material, industry grade soda ash and hydrated lime were investigated as solid activators in order to activate a silica fume blended slag mix. A “just add water” methodology was followed to meet the site requirements. The strength development, and the microstructural analysis to support the same were performed. Also, a side-by-side comparison was also done. Follow-up compressive strength tests were also performed on control samples and pre-mixed soda ash in water samples to tally the corresponding 7-day and 28-day strengths, as the current investigation claimed to establish the mix to give comparable, if not better, results.

The study brings out the following findings:

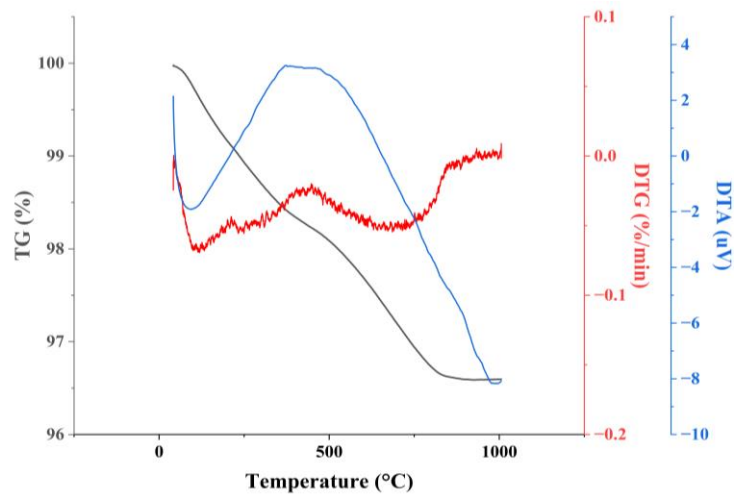
- (i) For a 10% SF addition and a 10% targeted NaOH content, the mixes showed highest strength development. The mix demonstrated 35.1 MPa after 28 days and 41.33 MPa after 120 days, making it suitable for use as a structural material. The corresponding initial strength for the control mix was low. At 28 days, the strength was comparable for mixes activated by a pre-mixed solution of NaOH (analytical grade). Mixes activated by a pre-mixed soda ash solution showed higher 28-day strength compared to the solid-state mixes. In all states, though, 10% SF and 10% NaOH showed the maximum strength development.
- (ii) At 28 days, the XRD intensities of portlandite, calcite, and brucite were either reduced or disappeared. The presence of magnesian calcite, magnesite, and hydrotalcite was detected, which aided in strength gain by supplying Ca^{+2} for secondary reactions and the subsequent formation of CNASH; the presence of which was detected in the XRD of samples after 28 days of curing.
- (iii) The SEM images show that, while CaCO_3 dominated the microstructure at 7 days, a denser microstructure developed at 28 days, which aided in the development of strength.
- (iv) Later-age samples were found to contain magnesian calcite as well as magnesite, according to EDS analysis. The TG-DT analysis also provided the same insights.
- (v) The TG-DT curves, in addition to providing a summary of the phase transitions, also provided an estimate of the bound water associated with the hydration products. Despite the presence of free water and hydroxides, SF10NH10 demonstrated higher strength due to calcite transitioning into magnesian calcite and portlandite supplanting CNASH and CSH.

Thus, dry direct mixing of commercially available activators with the precursors is a feasible alternative to the premixing of the analytical grade activators providing comparable strength. The end products are slightly different and advantageous to strength-gain. Chemicals of the corresponding industrial grade were found to have provided a similar strength development as the analytical ones. Ambient curing methods can be used, since it is a more site-convenient option. Overall, this one-part combination could serve as a proper cost-effective site-friendly binder. More research is needed and intended, to design a concrete mix using the binder, and study the performance-based properties.

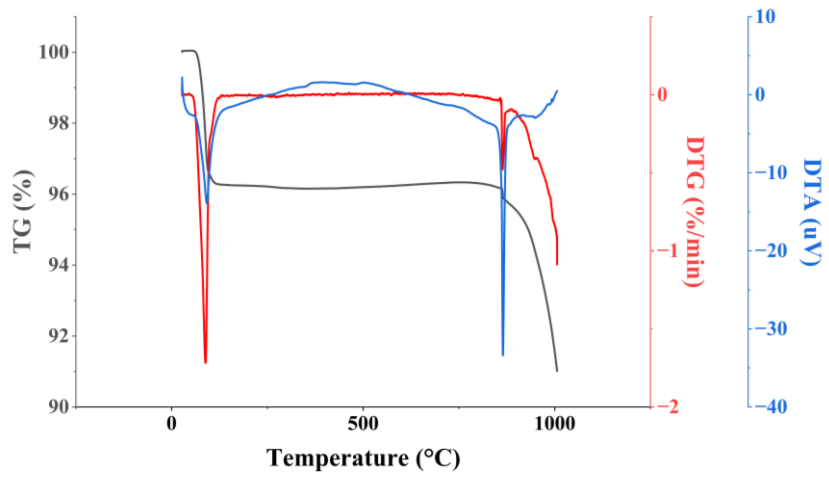
Appendix A



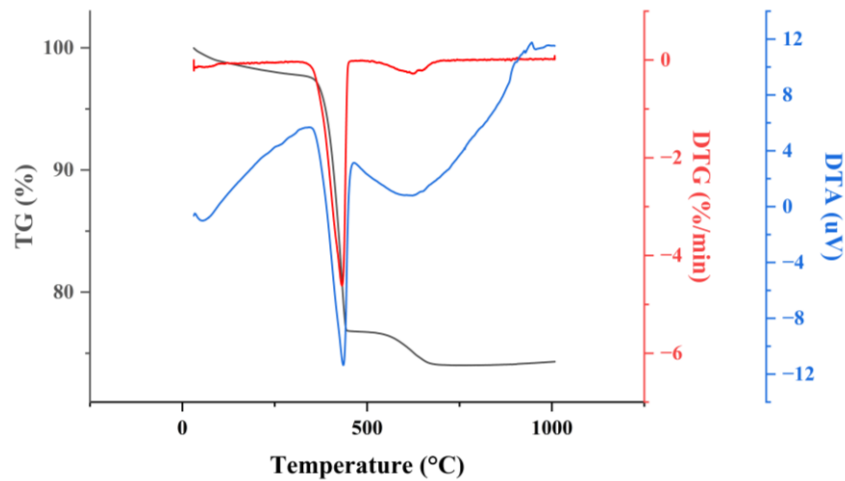
(a)



(b)



(c)



(d)

Figure 12: TG-DTG and DTA curves for (a) GGBFS, (b) SF, (c) SA, and (d) HL respectively.

Disclosure Statement

The authors report there are no competing interests to declare.

References

- [1] M. D. Jackson *et al.*, 'Phillipsite and Al-tobermorite mineral cements produced through low-temperature water-rock reactions in Roman marine concrete', *American Mineralogist*, vol. 102, no. 7, 2017, doi: 10.2138/am-2017-5993CCBY.
- [2] L. M. Seymour, N. Tamura, M. D. Jackson, and A. Masic, 'Reactive binder and aggregate interfacial zones in the mortar of Tomb of Caecilia Metella concrete, 1C BCE, Rome', *Journal of the American Ceramic Society*, vol. 105, no. 2, 2022, doi: 10.1111/jace.18133.
- [3] C. Shi, A. F. Jiménez, and A. Palomo, 'New cements for the 21st century: The pursuit of an alternative to Portland cement', *Cement and Concrete Research*, vol. 41, no. 7. Elsevier Ltd, pp. 750–763, 2011. doi: 10.1016/j.cemconres.2011.03.016.
- [4] J. L. Provis, 'Alkali-activated materials', *Cement and Concrete Research*, vol. 114. Elsevier Ltd, pp. 40–48, Dec. 01, 2018. doi: 10.1016/j.cemconres.2017.02.009.
- [5] D. J. M. Flower and J. G. Sanjayan, 'Green house gas emissions due to concrete manufacture', *Int J Life Cycle Assess*, vol. 12, no. 5, 2007, doi: 10.1007/s11367-007-0327-3.
- [6] M. Wu *et al.*, 'Reducing environmental impacts and carbon emissions: Study of effects of superfine cement particles on blended cement containing high volume mineral admixtures', *J Clean Prod*, vol. 196, pp. 358–369, Sep. 2018, doi: 10.1016/J.JCLEPRO.2018.06.079.
- [7] S. H. Teh, T. Wiedmann, A. Castel, and J. de Burgh, 'Hybrid life cycle assessment of greenhouse gas emissions from cement, concrete and geopolymer concrete in Australia', *J Clean Prod*, vol. 152, pp. 312–320, May 2017, doi: 10.1016/J.JCLEPRO.2017.03.122.
- [8] C. K. Yip, G. C. Lukey, and J. S. J. van Deventer, 'The coexistence of geopolymeric gel and calcium silicate hydrate at the early stage of alkaline activation', *Cem Concr Res*, vol. 35, no. 9, 2005, doi: 10.1016/j.cemconres.2004.10.042.
- [9] D. Hardjito and B. V. Rangan, 'Development and properties of low-calcium fly ash-based geopolymer concrete', 2005.
- [10] V. Nežerka, P. Bílý, V. Hrbek, and J. Fládr, 'Impact of silica fume, fly ash, and metakaolin on the thickness and strength of the ITZ in concrete', *Cem Concr Compos*, vol. 103, 2019, doi: 10.1016/j.cemconcomp.2019.05.012.
- [11] M. Rostami and K. Behfarnia, 'The effect of silica fume on durability of alkali activated slag concrete', *Constr Build Mater*, vol. 134, 2017, doi: 10.1016/j.conbuildmat.2016.12.072.
- [12] L. Li, H. A. Ali, J. xin Lu, and C. S. Poon, 'Role of silica fume in alkali-activated slag/glass powder paste', *Constr Build Mater*, vol. 356, p. 129189, Nov. 2022, doi: 10.1016/J.CONBUILDMAT.2022.129189.
- [13] S. H. Kang, Y. H. Kwon, S. G. Hong, S. Chun, and J. Moon, 'Hydrated lime activation on byproducts for eco-friendly production of structural mortars', *J Clean Prod*, vol. 231, 2019, doi: 10.1016/j.jclepro.2019.05.313.
- [14] X. Dai, S. Aydın, M. Y. Yardımcı, K. Lesage, and G. De Schutter, 'Rheology and microstructure of alkali-activated slag cements produced with silica fume activator', *Cem Concr Compos*, vol. 125, Jan. 2022, doi: 10.1016/J.CEMCONCOMP.2021.104303.

- [15] C. B. Cheah, L. E. Tan, and M. Ramli, 'The engineering properties and microstructure of sodium carbonate activated fly ash/slag blended mortars with silica fume', *Compos B Eng*, vol. 160, 2019, doi: 10.1016/j.compositesb.2018.12.056.
- [16] 'Sodium hydroxide CAS 1310-73-2 | 106462'. https://www.merckmillipore.com/IN/en/product/Sodium-hydroxide,MDA_CHEM-106462 (accessed Mar. 31, 2023).
- [17] 'Sodium carbonate CAS 497-19-8 | 106392'. https://www.merckmillipore.com/IN/en/product/Sodium-carbonate,MDA_CHEM-106392 (accessed Mar. 31, 2023).
- [18] 'Calcium hydroxide CAS 1305-62-0 | 102047'. https://www.merckmillipore.com/IN/en/product/Calcium-hydroxide,MDA_CHEM-102047 (accessed Mar. 31, 2023).
- [19] 'Price list for Soda Ash'. <https://www.tatachemicals.com/price-list-for-soda-ash> (accessed Mar. 31, 2023).
- [20] 'hydrated lime - Shreeram Chemical Industries'. <https://www.indiamart.com/shreeramchemicalindustries/search.html?ss=hydrated+lime> (accessed Mar. 31, 2023).
- [21] J. Ren *et al.*, 'Experimental comparisons between one-part and normal (two-part) alkali-activated slag binders', *Constr Build Mater*, vol. 309, Nov. 2021, doi: 10.1016/J.CONBUILDMAT.2021.125177.
- [22] H. G. Brittain and R. D. Bruce, 'Chapter 4 Thermal analysis', *Comprehensive Analytical Chemistry*, vol. 47, 2006, doi: 10.1016/S0166-526X(06)47004-5.
- [23] B. Akturk, S. Nayak, S. Das, and A. B. Kizilkanat, 'Microstructure and Strength Development of Sodium Carbonate-Activated Blast Furnace Slags', *Journal of Materials in Civil Engineering*, vol. 31, no. 11, Nov. 2019, doi: 10.1061/(asce)mt.1943-5533.0002944.
- [24] S. A. Bernal, J. L. Provis, R. J. Myers, R. San Nicolas, and J. S. J. van Deventer, 'Role of carbonates in the chemical evolution of sodium carbonate-activated slag binders', *Materials and Structures/Materiaux et Constructions*, vol. 48, no. 3, 2014, doi: 10.1617/s11527-014-0412-6.
- [25] C. Ma, B. Zhao, S. Guo, G. Long, and Y. Xie, 'Properties and characterization of green one-part geopolymer activated by composite activators', *J Clean Prod*, vol. 220, pp. 188–199, May 2019, doi: 10.1016/j.jclepro.2019.02.159.
- [26] J. Wang, X. J. Lyu, L. Wang, X. Cao, Q. Liu, and H. Zang, 'Influence of the combination of calcium oxide and sodium carbonate on the hydration reactivity of alkali-activated slag binders', *J Clean Prod*, vol. 171, 2018, doi: 10.1016/j.jclepro.2017.10.077.
- [27] S. Alonso and A. Palomo, 'Alkaline activation of metakaolin and calcium hydroxide mixtures: Influence of temperature, activator concentration and solids ratio', *Mater Lett*, vol. 47, no. 1–2, 2001, doi: 10.1016/S0167-577X(00)00212-3.
- [28] Z. Li, S. Zhang, Y. Zuo, W. Chen, and G. Ye, 'Chemical deformation of metakaolin based geopolymer', *Cem Concr Res*, vol. 120, 2019, doi: 10.1016/j.cemconres.2019.03.017.
- [29] K. M. L. Alventosa and C. E. White, 'The effects of calcium hydroxide and activator chemistry on alkali-activated metakaolin pastes', *Cem Concr Res*, vol. 145, 2021, doi: 10.1016/j.cemconres.2021.106453.
- [30] Z. Jiao, Y. Wang, W. Zheng, and W. Huang, 'Effect of dosage of sodium carbonate on the strength and drying shrinkage of sodium hydroxide based alkali-activated slag paste', *Constr Build Mater*, vol. 179, 2018, doi: 10.1016/j.conbuildmat.2018.05.194.
- [31] A. F. Abdalqader, F. Jin, and A. Al-Tabbaa, 'Development of greener alkali-activated cement: Utilisation of sodium carbonate for activating slag and fly ash mixtures', *J Clean Prod*, vol. 113, 2016, doi: 10.1016/j.jclepro.2015.12.010.
- [32] K. Scrivener, R. Snellings, and B. Lothenbach, *A practical guide to microstructural analysis of cementitious materials*, 2016th ed. CRC Press Taylor & Francis Group.
- [33] O. Abdelrahman and N. Garg, 'Impact of Na/Al Ratio on the Extent of Alkali-Activation Reaction: Non-linearity and Diminishing Returns', *Front Chem*, vol. 9, Jan. 2022, doi: 10.3389/fchem.2021.806532.
- [34] Raúl Fernández, A. I. Ruiz, and J. Cuevas, 'Formation of C-A-S-H phases from the interaction between concrete or cement and bentonite', *Clay Miner*, vol. 51, no. 2, 2016, doi: 10.1180/claymin.2016.051.2.09.
- [35] P. de Silva, L. Bucea, and V. Sirivatnanon, 'Chemical, microstructural and strength development of calcium and magnesium carbonate binders', *Cem Concr Res*, vol. 39, no. 5, 2009, doi: 10.1016/j.cemconres.2009.02.003.
- [36] B. Adeleke, J. Kinuthia, and J. Oti, 'Optimization of MgO-GGBS cementitious systems using thermo-chemical approaches', *Sustainability (Switzerland)*, vol. 13, no. 16, 2021, doi: 10.3390/su13169378.
- [37] M. ben Haha, B. Lothenbach, G. le Saout, and F. Winnefeld, 'Influence of slag chemistry on the hydration of alkali-activated blast-furnace slag - Part I: Effect of MgO', *Cem Concr Res*, vol. 41, no. 9, 2011, doi: 10.1016/j.cemconres.2011.05.002.
- [38] B. Walkley, R. San Nicolas, M. A. Sani, S. A. Bernal, J. S. J. van Deventer, and J. L. Provis, 'Structural evolution of synthetic alkali-activated CaO-MgO-Na₂O-Al₂O₃-SiO₂ materials is influenced by Mg content', *Cem Concr Res*, vol. 99, pp. 155–171, Sep. 2017, doi: 10.1016/J.CEMCONRES.2017.05.006.
- [39] H. T. Schaefer, C. F. Windisch, B. P. McGrail, P. F. Martin, and K. M. Rosso, 'Brucite [Mg(OH)₂] carbonation in wet supercritical CO₂: An in situ high pressure X-ray diffraction study', *Geochim Cosmochim Acta*, vol. 75, no. 23, 2011, doi: 10.1016/j.gca.2011.09.029.
- [40] S. D. Wang and K. L. Scrivener, 'Hydration products of alkali activated slag cement', *Cem Concr Res*, vol. 25, no. 3, 1995, doi: 10.1016/0008-8846(95)00045-E.
- [41] M. Kovtun, E. P. Kearsley, and J. Shekhovtsova, 'Chemical acceleration of a neutral granulated blast-furnace slag activated by sodium carbonate', *Cem Concr Res*, vol. 72, pp. 1–9, Jun. 2015, doi: 10.1016/j.cemconres.2015.02.014.
- [42] G. Montes-Hernandez, N. Findling, and F. Renard, 'Dissolution-precipitation reactions controlling fast formation of dolomite under hydrothermal conditions', *Applied Geochemistry*, vol. 73, 2016, doi: 10.1016/j.apgeochem.2016.08.011.
- [43] E. B. Barbara, L. Daniel, R. Alexander, and G. F. Winnefeld, 'Effect of carbonates on the formation of magnesium silicate hydrates', *Mater Struct*, vol. 55, 2018, doi: 10.1617/s11527-022-02018-3.

- [44] E. Bernard, B. Lothenbach, I. Pochard, and C. Cau-Dit-Coumes, 'Alkali binding by magnesium silicate hydrates', *Journal of the American Ceramic Society*, vol. 102, no. 10, 2019, doi: 10.1111/jace.16494.
- [45] L. Monasterio-Guillot, A. Fernandez-Martinez, E. Ruiz-Agudo, and C. Rodriguez-Navarro, 'Carbonation of calcium-magnesium pyroxenes: Physical-chemical controls and effects of reaction-driven fracturing', *Geochim Cosmochim Acta*, vol. 304, 2021, doi: 10.1016/j.gca.2021.02.016.
- [46] S. A. Bernal, E. D. Rodríguez, R. Mejía De Gutiérrez, M. Gordillo, and J. L. Provis, 'Mechanical and thermal characterisation of geopolymers based on silicate-activated metakaolin/slag blends', *J Mater Sci*, vol. 46, no. 16, 2011, doi: 10.1007/s10853-011-5490-z.
- [47] T. Nochaiya, W. Wongkeo, K. Pimraksa, and A. Chaipanich, 'Microstructural, physical, and thermal analyses of Portland cement-fly ash-calcium hydroxide blended pastes', *J Therm Anal Calorim*, vol. 100, no. 1, 2010, doi: 10.1007/s10973-009-0491-8.
- [48] L. Alarcon-Ruiz, G. Platret, E. Massieu, and A. Ehrlicher, 'The use of thermal analysis in assessing the effect of temperature on a cement paste', *Cem Concr Res*, vol. 35, no. 3, 2005, doi: 10.1016/j.cemconres.2004.06.015.
- [49] A. Palomo, P. Krivenko, I. Garcia-Lodeiro, E. Kavalerova, O. Maltseva, and A. Fernández-Jiménez, 'A review on alkaline activation: New analytical perspectives', *Materiales de Construcción*, vol. 64, no. 315, 2014, doi: 10.3989/mc.2014.00314.
- [50] M. Criado, W. Aperador, and I. Sobrados, 'Microstructural and mechanical properties of alkali activated Colombian raw materials', *Materials*, vol. 9, no. 3, 2016, doi: 10.3390/ma9030158.
- [51] D. Redaoui, F. Sahnoune, M. Heraiz, and A. Raghdi, 'Mechanism and kinetic parameters of the thermal decomposition of gibbsite Al(OH)₃ by thermogravimetric analysis', in *Acta Physica Polonica A*, 2017. doi: 10.12693/APhysPolA.131.562.
- [52] J. A. Wang *et al.*, 'Characterizations of the thermal decomposition of brucite prepared by sol-gel technique for synthesis of nanocrystalline MgO', *Mater Lett*, vol. 35, no. 5–6, 1998, doi: 10.1016/S0167-577X(97)00273-5.
- [53] A. A. Amer, 'Thermal analysis of hydrated fly ash-lime pastes', *J Therm Anal Calorim*, vol. 54, no. 3, 1998, doi: 10.1023/A:1010100222075.
- [54] S. A. Abo-El-Enein, F. I. El-Hosiny, S. M. A. El-Gamal, M. S. Amin, and M. Ramadan, 'Gamma radiation shielding, fire resistance and physicochemical characteristics of Portland cement pastes modified with synthesized Fe₂O₃ and ZnO nanoparticles', *Constr Build Mater*, vol. 173, 2018, doi: 10.1016/j.conbuildmat.2018.04.071.
- [55] R. S. Mikhail, S. Brunauer, and L. E. Copeland, 'Kinetics of the thermal decomposition of calcium hydroxide', *J Colloid Interface Sci*, vol. 21, no. 4, 1966, doi: 10.1016/0095-8522(66)90005-5.
- [56] X. Gao, Q. L. Yu, and H. J. H. Brouwers, 'Reaction kinetics, gel character and strength of ambient temperature cured alkali activated slag-fly ash blends', *Constr Build Mater*, vol. 80, 2015, doi: 10.1016/j.conbuildmat.2015.01.065.
- [57] K. Garbev, M. Bornefeld, G. Beuchle, and P. Stemmermann, 'Cell dimensions and composition of nanocrystalline calcium silicate hydrate solid solutions. Part 2: X-ray and thermogravimetry study', *Journal of the American Ceramic Society*, vol. 91, no. 9, 2008, doi: 10.1111/j.1551-2916.2008.02601.x.
- [58] E. Tajuelo Rodriguez, K. Garbev, D. Merz, L. Black, and I. G. Richardson, 'Thermal stability of C-S-H phases and applicability of Richardson and Groves' and Richardson C-(A)-S-H(I) models to synthetic C-S-H', *Cem Concr Res*, vol. 93, 2017, doi: 10.1016/j.cemconres.2016.12.005.
- [59] H. Song, Y. Jeong, S. Bae, Y. Jun, S. Yoon, and J. Eun Oh, 'A study of thermal decomposition of phases in cementitious systems using HT-XRD and TG', *Constr Build Mater*, vol. 169, 2018, doi: 10.1016/j.conbuildmat.2018.03.001.
- [60] I. Hager, M. Sitarz, and K. Mróz, 'Fly-ash based geopolymer mortar for high-temperature application – Effect of slag addition', *J Clean Prod*, vol. 316, 2021, doi: 10.1016/j.jclepro.2021.128168.
- [61] R. M. McIntosh, J. H. Sharp, and F. W. Wilburn, 'The thermal decomposition of dolomite', *Thermochim Acta*, vol. 165, no. 2, 1990, doi: 10.1016/0040-6031(90)80228-Q.
- [62] J. I. Bhatti, 'Hydration versus strength in a portland cement developed from domestic mineral wastes - a comparative study', *Thermochim Acta*, vol. 106, no. C, 1986, doi: 10.1016/0040-6031(86)85120-6.
- [63] I. Pane and W. Hansen, 'Investigation of blended cement hydration by isothermal calorimetry and thermal analysis', *Cem Concr Res*, vol. 35, no. 6, 2005, doi: 10.1016/j.cemconres.2004.10.027.
- [64] S. M. Monteagudo, A. Moragues, J. C. Gálvez, M. J. Casati, and E. Reyes, 'The degree of hydration assessment of blended cement pastes by differential thermal and thermogravimetric analysis. Morphological evolution of the solid phases', *Thermochim Acta*, vol. 592, 2014, doi: 10.1016/j.tca.2014.08.008.
- [65] W. Deboucha, N. Leklou, A. Khelidj, and M. N. Oudjit, 'Hydration development of mineral additives blended cement using thermogravimetric analysis (TGA): Methodology of calculating the degree of hydration', *Constr Build Mater*, vol. 146, 2017, doi: 10.1016/j.conbuildmat.2017.04.132.
- [66] J. Rivera Lozano, 'Hidratación de pastas de cemento de con adiciones activas|subproductos industriales y materiales de desecho', Universidad Autónoma de Madrid, 2004.
- [67] A. Bessa, 'Study of the contribution of mineral additions to the physical and mechanical durability of mortars.', University of Cergy-Pontoise, France, 2004.
- [68] Y. Zhang, Q. Zhao, Z. Gao, and J. Chang, 'Microstructure Control of AH3Gel Formed in Various Calcium Sulfoaluminate Cements as a Function of pH', *ACS Sustain Chem Eng*, vol. 9, no. 34, pp. 11534–11547, Aug. 2021, doi: 10.1021/acssuschemeng.1c03886.